Molecular Therapy
Nucleic Acids
Original Article

A DNA/RNA heteroduplex oligonucleotide coupling asparagine depletion restricts FGFR2 fusion-driven intrahepatic cholangiocarcinoma

Zhenzhen Chu,[1,8] Baohuan Zhang,[2,8] Xuxuan Zhou,[1,8] Hui Yuan,[6,8] Chongqing Gao,[1] Lihao Liu,[4] Yang Xiao,[3] Jichun Zhang,[5] Jian Hong,[1,3] Junjie Liang,[3] Dong Chen,[7] and Nan Yao[1]

[1]Department of Pathophysiology, School of Medicine, Jinan University, Guangzhou, Guangdong 510632, China; [2]Morphology Experimental Teaching Center, School of Medicine, Jinan University, Guangzhou, Guangdong 510632, China; [3]Department of Hepatobiliary Surgery, the First Affiliated Hospital, Jinan University, Guangzhou, Guangdong 510632, China; [4]School of Medicine, Jinan University, Guangzhou, Guangdong 510632, China; [5]Department of Physiology, School of Medicine, Jinan University, Guangzhou, Guangdong 510632, China; [6]Department of Gastroenterology, Huizhou Municipal Central Hospital, Huizhou, Guangdong 516001, China; [7]Department of Pancreato-Biliary Surgery, the First Affiliated Hospital, Sun Yat-sen University, Guangzhou, Guangdong 510080, China

Pemigatinib, a pan-FGFR inhibitor, is approved to treat intrahepatic cholangiocarcinoma (ICC) harboring FGFR2 fusion mutations. Improving its targeting of FGFR2 fusions remains an unmet clinical need due to its pan selectivity and resistance. Here, we report a cholesterol-conjugated DNA/RNA heteroduplex oligonucleotide targeting the chimeric site in *FGFR2-AHCYL1* (F-A Cho-HDO) that accumulates in ICC through endocytosis of low-density lipoprotein receptor (LDLR), which is highly expressed in both human and murine ICC. F-A Cho-HDO was determined to be a highly specific, sustainable, and well-tolerated agent for inhibiting ICC progression through posttranscriptional suppression of F-A in ICC patient-derived xenograft mouse models. Moreover, we identified an EGFR-orchestrated bypass signaling axis that partially offset the efficacy of F-A Cho-HDO. Mechanistically, EGFR-induced STAT1 upregulation promoted asparagine (Asn) synthesis through direct transcriptional upregulation of asparagine synthetase (ASNS) and dictated cell survival by preventing p53-dependent cell cycle arrest. Asn restriction with ASNase or ASNS inhibitors reduced the intracellular Asn, thereby reactivating p53 and sensitizing ICC to F-A Cho-HDO. Our findings highlight the application of genetic engineering therapies in ICC harboring FGFR2 fusions and reveal an axis of adaptation to FGFR2 inhibition that presents a rationale for the clinical evaluation of a strategy combining FGFR2 inhibitors with Asn depletion.

INTRODUCTION

Intrahepatic cholangiocarcinoma (ICC), a subtype of cholangiocarcinoma (CCA) that arises from the intrahepatic biliary tract, is the second most common primary hepatic malignancy, after only hepatocellular carcinoma.[1,2] It is often diagnosed in advanced stages, in which gemcitabine and cisplatin combination therapy is currently considered the standard of care.[3,4] However, the various side effects and frequent drug resistance limit its clinical implementation.[5] There is no established standard of care following first-line chemotherapy failure, and clinically approved second-line agents are also few and less effective.[6] In addition, due to the complex unclear pathogenesis of ICC, there are fewer clinically approved targeted therapeutics. Therefore, ICC remains a complex problem, and the exploration of effective targeted treatment options is urgently needed.

Despite the high heterogeneity and complex pathogenesis of ICC, next-generation sequencing analyses are providing new insights into the mechanisms of ICC and determining the spectrum of therapeutic targets.[7,8] Genomic analysis of patients with ICC has revealed alterations in targetable oncogenes in almost 44% of patients.[9] Among the genetic aberrations, FGFR2 fusion mutations are present in ~14% of ICCs, and the encoded proteins have been well established as targetable molecules.[10] *FGFR2-AHCYL1* (henceforth abbreviated as F-A) is a common FGFR2 fusion that has been identified in ICC.[11] This mutation generates the FGFR2 oncogenic driver by constitutively stimulating the MAPK pathway and leads to excessive proliferation of tumor cells.[12,13] This tumorigenic ability was found to be attributable to its kinase activity.[14] Pemigatinib was the first selective pan-FGFR kinase inhibitor approved by the Food and Drug Administration and the European Medicines Agency for the treatment of advanced CCA with FGFR2 fusion mutation.[15] Notably, after a median follow-up of 17.8 months, 35.5% (38 of 107) of patients

Received 25 May 2023; accepted 29 September 2023;
https://doi.org/10.1016/j.omtn.2023.102047.

[8]These authors contributed equally

Correspondence: Junjie Liang, Department of Hepatobiliary Surgery, the First Affiliated Hospital, Jinan University, Guangzhou, Guangdong 510632, China.
E-mail: jjliang@jnu.edu.cn
Correspondence: Dong Chen, Department of Pancreato-Biliary Surgery, the First Affiliated Hospital, Sun Yat-sen University, Guangzhou, Guangdong 510080, China.
E-mail: chend9@mail.sysu.edu.cn
Correspondence: Nan Yao, Department of Pathophysiology, School of Medicine, Jinan University, Guangzhou, Guangdong 510632, China.
E-mail: yaon107@jnu.edu.cn

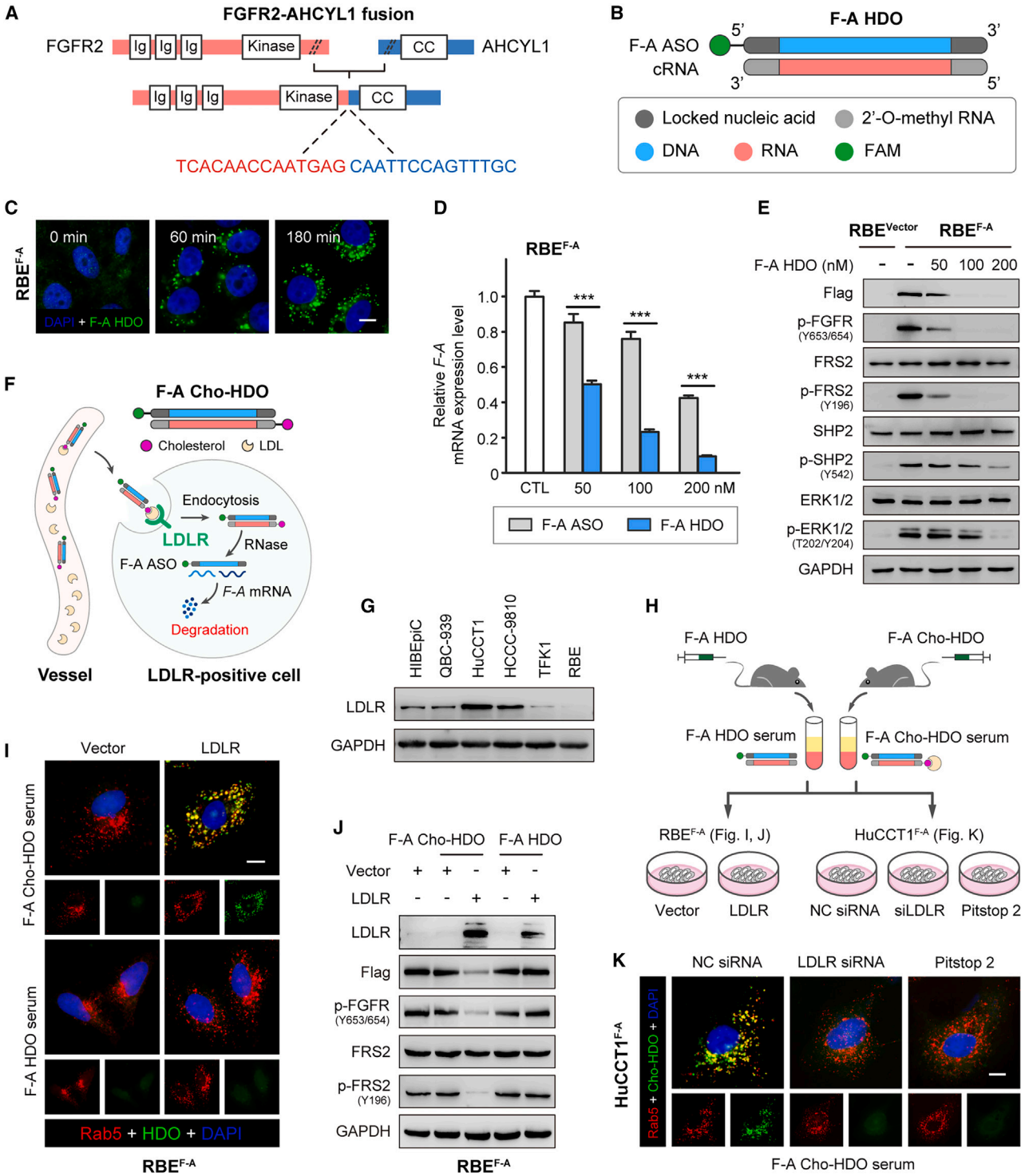

Figure 1. Design of the F-A Cho-HDO that can be internalized by ICC cells through LDLR-mediated endocytosis

(A) Schematic of the *F-A* fusion gene. (B) Schematic illustration of F-A HDO. (C) The internalization of F-A HDO (200 nM) in RBE^{F-A} cells was visualized by confocal microscopy at 0 min, 60 min, and 180 min. Scale bar, 10 μm. (D) RT-qPCR analysis of relative *F-A* mRNA levels in RBE^{F-A} cells after transfection with F-A HDO or F-A ASO for 48 h. ***$p < 0.001$. (E) Western blot analysis of the protein levels of F-A (flag), p-FGFR2, and its downstream factors in RBE^{vector} and RBE^{F-A} cells after treatment with F-A HDO for 48 h. (F) Schematic diagram of F-A Cho-HDO and how F-A Cho-HDO enters LDLR-positive cells. (G) Western blot analysis of LDLR expression in various CCA cell lines. (H)

(legend continued on next page)

harboring FGFR2 fusions or rearrangements showed an objective response,[16] with several patients with CCA achieving a complete response and a median duration of treatment of 7.5 months.[17] However, indiscriminate targeting of wild-type (WT) FGFR leads to a treatment-related adverse effect, including hyperphosphatemia (75%), stomatitis (29.7%), or fatigue (23.4%), in 90% of ICC patients, which affects their quality of life.[18] Furthermore, tumors can acquire resistance to FGFR inhibitors mediated chiefly by alternative pathway activation, such as overexpression of Erk1/2 via amplification and activation of AKT, which limits the durable benefit of pemigatinib.[19,20] Inhibitors that target these alternative pathways, such as ERK inhibitors, are effective in reversing acquired resistance to FGFR2 inhibitors.[21] Therefore, exploring more effective targeted therapy and even combination therapy strategies directed against FGFR2 fusion mutations may optimize FGFR2 pathway suppression and prolong the clinical benefit in ICC patients with FGFR2 alterations.

Nucleotide-based drugs, such as antisense oligonucleotides (ASOs), have recently experienced rapid success in clinical translation.[22,23] Their advantage lies in their improved specificity and almost unlimited ability to target any genetically encoded material,[24] especially those that cannot be targeted by other types of drugs, such as small molecules and antibodies. Prof. Takanori Yokota developed a new class of ASO, DNA-RNA heteroduplex oligonucleotides (HDOs), in which a single-stranded ASO is duplexed with a complementary RNA (cRNA) that is further conjugated to cholesterol (Cho).[25,26] Compared with the parent single-stranded gapmer ASOs, HDOs are significantly more potent in reducing the expression of the targeted mRNA and have lower immunoreactivity.[25] In addition, they are not readily degraded by nucleases in the blood circulation due to their DNA-RNA duplexes. These properties make them potentially useful in treating diseases with known genetic drivers. However, the specific delivery of nucleotide-based drugs to lesion sites is a great challenge due to nuclease degradation and the presence of various physiological and biological barriers.[27] The low-density lipoprotein receptor (LDLR) is an efficient internal uptake recycling receptor with a recycling rate of approximately 10 min and a lifetime of 24 h.[28,29] Given the advantages of a high number of LDLRs on the surface of hepatocytes and a short circulation time, cholesterol has widely been used as an ideal conjugate for hepatocyte-targeted nucleic acid drugs.[30] However, whether LDLR is also highly expressed in ICC and whether the Cho-HDO conjugate can be an ideal strategy for ICC-targeted therapy are rarely reported.

In the present study, we found that high expression of LDLR is common between human and mouse ICC and mediates the accumulation of a cholesterol-conjugated DNA/RNA heteroduplex oligonucleotide targeting the chimeric site in *FGFR2-AHCYL1* (F-A Cho-HDO) at the tumor site, thereby suppressing F-A-driven ICC progression. Moreover, transcriptome sequencing revealed that F-A Cho-HDO treatment also led to the activation of several bypass signaling axes. Upregulation of asparagine synthetase (ASNS) was pronounced among these activations and promoted ICC progression through asparagine (Asn)-mediated p53 suppression. Combination treatment with F-A Cho-HDO and asparaginase (ASNase) (a clinical antitumor drug) achieved a better therapeutic effect than F-A Cho-HDO treatment alone. These studies provide new ideas for clinical ICC treatments involving genetically engineered therapies and a combination of FGFR2 inhibition and ASNase.

RESULTS

Design of the Cho-HDO targeting the chimeric region of F-A

F-A is one of the FGFR2 fusion mutations identified in ICC.[11,16] This chimeric gene consists of the in-frame fusion of the sequences encoding the *FGFR2* amino terminus (exons 1–19) and the *AHCYL1* carboxyl terminus (exons 5–21), which enhances receptor dimerization and kinase activity (Figure 1A). Pemigatinib is a potent FGFR inhibitor that prolongs the survival of ICC patients harboring the F-A fusion but still causes adverse effects due to its panselectivity. Therefore, targeting the chimeric region of F-A through genetic engineering may be a highly specific strategy to avoid targeting WT *FGFR2* or WT *AHCYL1*. In this study, we designed an HDO targeting the F-A fusion region (F-A HDO). As shown in Figure 1B, F-A HDO consists of an F-A antisense oligonucleotide (F-A ASO) strand and a cRNA strand. An FAM tag is fused to the 5′ end of the ASO for intracellular tracing. To obtain the F-A HDO with the best knockdown efficiency, we designed a set of 10 small interfering RNAs (siRNAs) with sequential tiling across the mutant *FGFR2-AHCYL1* junction (Figure S1A). The ICC cell line RBE, with low endogenous FGFR2 expression (Figure S1B), was transfected with F-A lentivirus to generate the stable RBE^{F-A} cell line, which was used to verify the knockdown efficiency. Through RT-qPCR analysis, we selected three potent siRNA sequences (#1, #3, and #5) with the highest knockdown efficiency to further synthesize three F-A HDOs (Figure S1C). Among these F-A HDOs, the most potent (F-A HDO #3, based on siRNA #3 and hereafter referred to as F-A HDO) was selected for further studies (Figure S1D). Through Lipofectamine 3000-mediated transfection, F-A HDO was rapidly internalized into RBE^{F-A} cells in a time-dependent manner (Figure 1C).

The predecessor of HDOs, ASOs are widely used for clinical treatment.[31,32] To compare the effect of F-A ASO and F-A HDO, we

Flowchart of the experimental strategy used in (I–K). (I) RBE^{F-A} cells transiently transfected with vector or LDLR plasmid were treated with F-A Cho-HDO-containing serum or F-A HDO-containing serum for 3 h. Intracellular F-A Cho-HDO, F-A HDO and their colocalization with rab5 were detected by immunofluorescence staining. Scale bar, 10 μm. (J) RBE^{F-A} cells transfected with vector or LDLR plasmid were treated with F-A Cho-HDO-containing serum or F-A HDO-containing serum for 48 h. The protein levels of indicated proteins were measured by western blot analysis. (K) HuCCT1^{F-A} cells transfected with NC siRNA or LDLR siRNA (400 nM) for 48 h or treated with pitstop 2 (20 μM) for 3 h were exposed to F-A Cho-HDO-containing serum for another 3 h. Intracellular F-A Cho-HDO and its colocalization with rab5 were detected by immunofluorescence staining. Scale bar, 10 μm.

treated RBE^{F-A} cells with both oligonucleotides using Lipofectamine 3000. After 48 h, F-A HDO showed more potent silencing of *F-A* mRNA than the parent F-A ASO (Figure 1D). In addition, F-A HDO treatment decreased the F-A protein level and the phosphorylation of FGFR2 in a dose-dependent manner (Figure 1E). Moreover, the downstream pro-survival pathways of FGFR2 and the phosphorylation of FRS2, SHP2, and ERK were also significantly inhibited[33] (Figure 1E). It is gratifying that F-A HDO did not downregulate WT *FGFR2* and *AHCYL1* in HuCCT1^{F-A} cells with endogenous FGFR2 (Figures S1B and S1E). The above results showed that targeting the chimeric region of FGFR2 fusions by HDO may be a potent and specific strategy to suppress FGFR2 activation. Lipofectamine 3000 is a modern transfection agent that is commonly used in molecular biological experiments, but it is not suitable for the *in vivo* delivery of oligonucleotides. Therefore, we further explored an effective way to deliver HDO to ICC cells.

The cholesterol-conjugated HDO (Cho-HDO) binds to LDL in plasma and enters the cells through LDLR endocytosis (Figure 1F). Since hepatocytes are rich in LDLR, Cho-HDOs have been widely used for the knockdown of specific genes in hepatocytes.[34] However, whether LDLR is also highly expressed on ICC cells has rarely been reported. We then explored the expression of LDLR in CCA cell lines and found that LDLR protein levels in the ICC cell lines HuCCT1 and HCCC-9810 were significantly higher than those in normal bile duct epithelial cells (HIBEpiC) or the extrahepatic cholangiocarcinoma (ECC) cell line QBC-939, while RBE cells and the ECC cell line TFK1 had almost undetectable LDLR expression (Figure 1G). Therefore, we speculated that Cho-HDO can also enter ICC cells through LDLR endocytosis. To verify this hypothesis, we synthesized an F-A Cho-HDO by coupling Cho to the 5′ end of a cRNA (Figure 1F) and injected this F-A Cho-HDO (40 mg/kg) or F-A HDO (40 mg/kg) into BALB/c mice via the tail vein. After circulation in the blood, F-A Cho-HDO bound to LDL to form F-A Cho-HDO-LDL complexes, while F-A HDO did not. Subsequently, serum from both groups of mice was collected and added to five groups of cells: RBE^{F-A} + Vector, RBE^{F-A} + LDLR; HuCCT1^{F-A} + NC siRNA, HuCCT1^{F-A} + siLDLR, and HuCCT1^{F-A} + pitstop 2 (Figure 1H). The results revealed that ectopic expression of LDLR in RBE^{F-A} cells significantly increased the accumulation of F-A Cho-HDO, which was found to be colocalized with Rab5, an early endosome marker. However, F-A HDO failed to enter RBE^{F-A} cells regardless of ectopic expression of LDLR (Figure 1I). Accordingly, F-A Cho-HDO effectively knocked down the expression of F-A and inhibited the phosphorylation of FGFR and the downstream protein FRS2 in LDLR-positive RBE^{F-A} cells, while F-A HDO had no such effect (Figure 1J). In addition, LDLR knockdown in HuCCT1^{F-A} cells with high LDLR expression (Figure S1F) significantly inhibited the enrichment of F-A Cho-HDO. Pitstop 2, a selective inhibitor of clathrin that modulates LDLR endocytosis, also blocked the entry of F-A Cho-HDO into HuCCT1^{F-A} cells (Figure 1K). The above results indicated that Cho-HDO could autonomously enter ICC cells through LDLR endocytosis in the absence of transfection reagents.

F-A Cho-HDO inhibits F-A-mediated malignant progression in ICC cell lines, patient-derived ICC cells, and organoids

To elucidate the anti-ICC effect of F-A Cho-HDO *in vitro*, four stable ICC cell lines, HuCCT1^{vector}, HuCCT1^{F-A}, HCCC-9810^{vector}, and HCCC-9810^{F-A}, were treated with F-A Cho-HDO using Lipofectamine 3000 reagent (this delivery method was used in all experiments as shown in Figure 2). The CCK-8 assay results showed that F-A Cho-HDO pretreatment dose-dependently inhibited F-A-driven ICC cell proliferation (Figure 2A). The colony formation assay results also demonstrated that knockdown of F-A by F-A Cho-HDO significantly suppressed the anchorage-dependent growth of ICC cells (Figure 2B). Inhibition of the FGFR2 pathway has been reported to induce cycle arrest and apoptosis.[35] We found that upon F-A Cho-HDO treatment, the apoptosis rate of ICC cells increased (Figure S1G), and the apoptosis-related proteins caspase-7, caspase-9, and PARP were cleaved, indicating apoptosis induction (Figure 2C). However, F-A Cho-HDO did not notably affect the cell cycle distribution (data not shown). The enhanced kinase activity mediated by FGFR2 fusion mutations also promotes the metastasis of ICC.[36] Therefore, the effect of F-A Cho-HDO on the invasion and migration abilities of ICC cells was further explored. We found nearly complete closure of the scratch in the F-A-positive ICC cells after 24 h relative to that at 0 h, indicating that F-A fusion increased the motility of ICC cells. However, this effect was suppressed by F-A Cho-HDO (Figure 2D). Consistent with this finding, the transwell assay results showed that F-A-positive ICC cells transfected with F-A Cho-HDO exhibited impaired migration and invasion (Figure 2E). These data indicated that ectopic expression of F-A promoted ICC cell migration and invasion, although these effects were abrogated by F-A Cho-HDO.

Although immortalized tumor cell lines cultured *in vitro* are widely used in scientific research, they have long been separated from the tumor microenvironment, and their properties do not accurately mimic those of tumor cells in patients.[37] Therefore, we obtained an ICC clinical sample, but there was no assurance that the sample contained *F-A* fusion mutations. Therefore, we isolated primary ICC cells from tumor tissue and induced the expression of the F-A fusion by lentiviral transduction (Figure 2F). Ectopic expression of F-A significantly promoted the proliferation of primary ICC cells, while F-A Cho-HDO treatment effectively reduced the levels of proteins in the FGFR2 pathway, including p-FGFR2, p-FRS2, p-SHP2, and p-ERK1/2, and suppressed ICC progression (Figures 2G and 2H). Compared with cancer cell lines cultured under monolayer conditions, 3D models reproduce a more accurate tumor proliferation pattern. Based on the concept of non-adherent coatings, we used ultra-low attachment plates to form patient-derived ICC spheroids (Figure 2F). The spheroid formation assay results demonstrated that F-A contributed to enhancing the sphere-forming ability compared with the vector and that F-A Cho-HDO decreased the sphere-forming ability of F-A-positive primary ICC cells (Figure 2I). These data indicated that sustained activation of FGFR2 by the F-A fusion mutation promotes ICC progression and that targeting F-A with F-A Cho-HDO effectively suppresses tumor progression in ICC cells harboring the F-A fusion mutation.

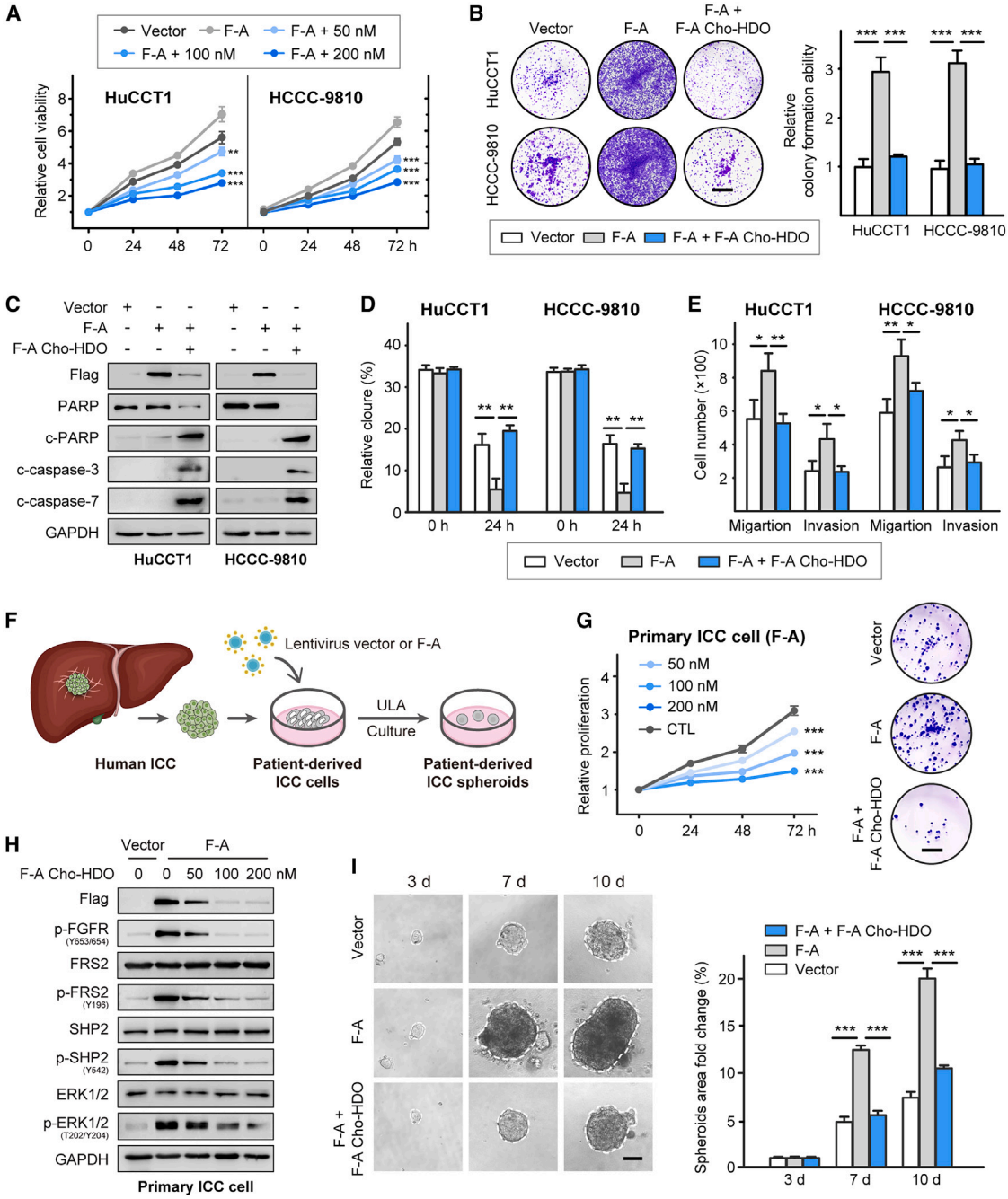

Figure 2. F-A Cho-HDO exerted an antitumor effect by depleting F-A in ICC cell lines, patient-derived ICC cells and spheroids

(A) Indicated ICC cell lines were pre-treated with F-A Cho-HDO for 48 h. Cell viability after a further 24, 48, or 72 h was measured by a CCK-8 assay. $^{**}p < 0.01$, $^{***}p < 0.001$ vs. the F-A group. (B) HuCCT1^{F-A} and HCCC-9810^{F-A} cells were pre-treated with F-A Cho-HDO (400 nM, 72 h) and subjected to a colony formation assay. Scale bar, 1 cm. $^{***}p < 0.001$. (C) HuCCT1^{F-A} and HCCC-9810^{F-A} cells were treated with 200 nM of F-A Cho-HDO for 48 h. The protein levels of the indicated apoptosis biomarkers were measured by western blot analysis. (D) HuCCT1^{F-A} and HCCC-9810^{F-A} cells were pre-treated with F-A Cho-HDO (200 nM, 48 h), and the migration ability was evaluated by a wound healing assay. $^{**}p < 0.01$. (E) HuCCT1^{F-A} and HCCC-9810^{F-A} cells were treated with F-A Cho-HDO (200 nM, 48 h) and subjected to transwell migration and invasion assays. $^{*}p < 0.05$, $^{**}p < 0.01$. (F) Schematic diagram of the establishment of F-A-positive patient-derived ICC cells and spheroids. (G) F-A-positive primary ICC cells were pre-treated with F-A Cho-HDO (200 nM) for 48 h. Then, cell viability was measured after another 24, 48, or 72 h by a CCK-8 assay (left), or a colony formation assay was performed (right). Scale bar, 1 cm, $^{***}p < 0.001$ vs. CTL. (H) F-A-positive primary ICC cells were treated with F-A Cho-HDO for 48 h. F-A, p-FGFR and downstream protein levels were measured by western blot analysis. (I) F-A-positive primary ICC cells were pre-treated with F-A Cho-HDO (400 nM, 72 h), and the sphere-forming ability was measured after 3, 7, and 10 days of culture under sphere-forming conditions. Scale bar, 50 μm. $^{***}p < 0.001$.

LDLR is highly expressed in spontaneous murine ICC and human ICC

We previously showed that LDLR was highly expressed in ICC cell lines (HuCCT1 and HCCC-9810), in which it mediated the endocytosis of F-A Cho-HDO. However, the expression characteristics of LDLR in ICC tissues remain unknown. To further explore whether F-A Cho-HDO can be effectively delivered to ICC tissues *in vivo*, we generated two spontaneous ICC models, namely, a diethylnitrosamine-left median bile duct ligation (DEN-LMBDL)-induced ICC mouse model and an oncogene-induced ICC mouse model, to evaluate whether LDLR is highly expressed in ICC tissues. DEN is currently the most widely used chemical to establish HCC models[38]; it contributes to liver damage and stimulates dysplasia of liver cells and bile duct epithelial cells, which, when combined with LMBDL, induces ICC. The schematic of model establishment is shown in Figure 3A. After 28 weeks, the mouse livers were removed for immunohistochemistry. Compared with paracancerous normal liver tissues, ICC tissues (CK19-positive) exhibited LDLR overexpression (n = 7) (Figure 3B). Clinical ICC can also originate from hepatocytes.[39] Therefore, we also established a mouse model of ICC driven by activated forms of the Akt (myr-Akt) and YapS127A proto-oncogenes, in which ICC developed from hepatocytes.[40,41] As shown in Figure 3C, we delivered Akt and YapS127 plasmids, along with Sleeping Beauty plasmids, into C57BL/6 mice through hydrodynamic tail vein injection (HDTV) to initiate ICC development. After 6 weeks of induction, the ICC foci were positive for CK19 and exhibited marked LDLR expression compared with the paracancerous tissues (Figure 3D). These results indicate that LDLR is highly expressed in spontaneous murine ICC models. Given that the murine ICC models do not fully reproduce human ICC, we also collected tumor tissues from ICC patients as the experimental cohort (n = 80) to investigate LDLR expression in human ICC. Consistent with the findings in the murine ICC models, LDLR exhibited high expression in human ICC (Figure 3E). For further validation, we selected an ICC tissue microarray (HIBD-Ade100PG-01, n = 76, Outdo Biotech, Shanghai, China) as the validation cohort to determine the expression level of LDLR. In this microarray, the expression of LDLR was observed in 98.7% (75 of 76) of the tumor tissues at different expression levels, and LDLR was more highly expressed in the tumor tissues than in the paracancerous tissues (Figure 3F). Based on this validation in rodent ICC models and human ICC samples, high expression levels of LDLR seem to be common in ICC. Thus, F-A Cho-HDO, targeting the F-A fusion mutation, is expected to be delivered to ICC sites through LDLR endocytosis *in vivo*.

F-A Cho-HDO is a highly specific, efficient, and well-tolerated strategy for targeting ICC in mouse models

To confirm whether F-A Cho-HDO can accumulate in ICC tissue, we further examined its biodistribution in mouse models. Nucleic acid drugs are clinically administered via intravenous (i.v.) injection and delivered to lesion sites through the peripheral circulation. Portal vein perfusion chemotherapy (PVC) is a highly transduction and well-targeted strategy for treating liver cancer that rapidly achieves high drug concentrations.[42] Therefore, we compared these two administration routes in mouse models. As shown in Figure 4A, BALB/c nude mice were administered the same dose of F-A Cho-HDO via tail i.v. injection or portal i.v. injection, and the livers were extracted for fluorescence detection of F-A Cho-HDO at 1 h and 6 h. At the same time point, significantly higher accumulation of F-A Cho-HDO in the liver was observed after portal vein injection than after tail vein administration, and F-A Cho-HDO was significantly enriched in hepatocytes within 1 h after portal vein injection, indicating that portal vein injection is indeed a highly effective method of hepatic drug delivery (Figure 4B).

Next, F-A Cho-HDO was injected via the tail or portal vein into BALB/c nude mice bearing orthotopic HuCCT1^{F-A} cell line-derived xenografts (CDXs) (LDLR-positive) or orthotopic RBE^{F-A} CDXs (LDLR-negative) to observe its biodistribution *in vivo*. Organs were excised 6 h after injection to analyze F-A Cho-HDO enrichment by fluorescence detection. We found that tail vein administration of F-A Cho-HDO caused significant accumulation in HuCCT1^{F-A} ICC tissue (CK19-positive) compared with peritumoral liver tissue due to the higher LDLR expression level in the ICC tissue (Figure 4C). In contrast, almost no F-A Cho-HDO was detected in orthotopic RBE^{F-A} CDXs (Figure S2A), further demonstrating that Cho-HDO enters cells through LDLR endocytosis. Additionally, weak F-A Cho-HDO fluorescence was also observed in kidney tissue, a phenomenon that may be related to renal clearance of HDO (Figure S2B). In contrast to F-A Cho-HDO administered via the tail vein, F-A Cho-HDO administered via the portal vein was detected almost only in the liver, and almost no Cho-HDO fluorescence was detected in other organs (Figure S2B). Moreover, for the same dose of F-A Cho-HDO, portal vein injection resulted in a higher F-A silencing efficiency than tail vein injection (Figure 4D). Thus, delivery of F-A Cho-HDO through the portal vein is expected to result in better specificity and higher efficiency. However, portal vein administration in rodents requires open surgery, which is harmful to rodents and cannot be performed repeatedly. Therefore, the subsequent experiments were continued using tail vein administration of F-A Cho-HDO. Moreover, in murine spontaneous ICC models, including the DEN-LMBDL-induced and the Akt-Yap-induced mouse ICC models, we detected a substantial amount of F-A Cho-HDO in ICC tissue after tail vein administration (Figure 4E).

The above data demonstrated that F-A Cho-HDO can be enriched in both ICC CDX and spontaneous mouse ICC tissues. We next verified whether F-A Cho-HDO can be enriched in human ICC tissues using an orthotopic ICC patient-derived xenograft (PDX) model. As shown in Figure 4F, we subcutaneously implanted a fresh LDLR-positive human ICC specimen (Figure S2C) into NOD-scid mice, and *F-A* adenovirus (AAV F-A) was intratumorally injected to induce F-A expression. After induction for 3 weeks, freshly harvested subcutaneous ICC tissues were digested into single-cell suspensions and implanted into the livers of new NOD-scid mice. F-A Cho-HDO or the corresponding F-A ASO was then delivered through the tail vein twice a week for 2 weeks. The ICC tissues were collected 1, 3, 7, 14, and 28 days after administration. F-A Cho-HDO was also enriched in human ICC tissues (CK19-positive) due to their LDLR

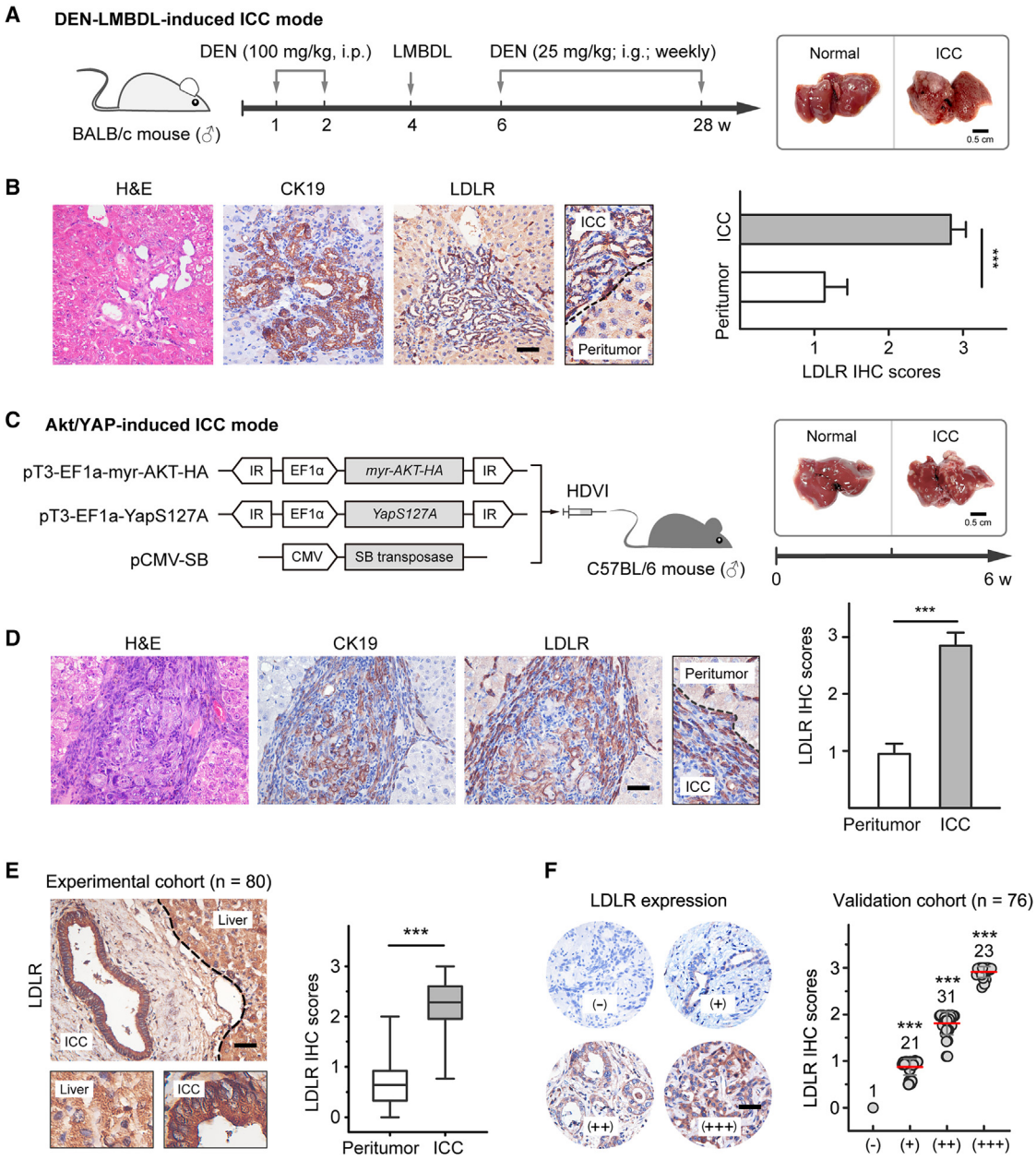

Figure 3. LDLR was highly expressed in spontaneous mouse ICC and human ICC samples

(A) Schematic of the DEN-LMBDL mouse ICC model and the morphology of normal liver and ICC tumor tissue in mice. (B) The representative images of H&E, CK19, and LDLR staining in DEN-LMBDL mouse ICC tissue and the statistical analysis of the LDLR IHC score (n = 7). Scale bar, 50 μm. ***p < 0.001. (C) Schematic diagram of the Akt/Yap-induced mouse ICC model and the morphology of normal liver and ICC tumor tissue from mice. (D) Representative images of H&E, CK19, and LDLR staining in liver tissue from mice with Akt/Yap-induced ICC and statistical analysis of the LDLR IHC score (n = 7). Scale bar, 50 μm. ***p < 0.001. (E) A representative image of LDLR IHC staining in paracancerous tissue and tumor tissue of an ICC patient and the statistical analysis of the LDLR IHC score in the experimental cohort (n = 80). Scale bar, 50 μm. ***p < 0.001. (F) Representative images of LDLR IHC staining in the validation cohort (n = 76) and statistical analysis of the data. Expression was classified as negative (−, n = 1); weakly positive (+, n = 21); moderately positive (++, n = 31) or strongly positive (+++, n = 23). Scale bar, 50 μm. ***p < 0.001 vs. the (−) group.

expression, as observed in the orthotopic ICC mouse model (Figure 4G). Moreover, the F-A silencing efficiency of F-A Cho-HDO was significantly higher and more durable (the F-A knockdown effect was sustained for nearly 1 month) than that of ASO (Figure 4H). The well performance of F-A Cho-HDO in terms of silencing efficiency and maintenance time *in vivo* is expected to allow reductions in the dose and frequency of administration, thereby minimizing side effects and improving patient compliance. We then treated normal BALB/c

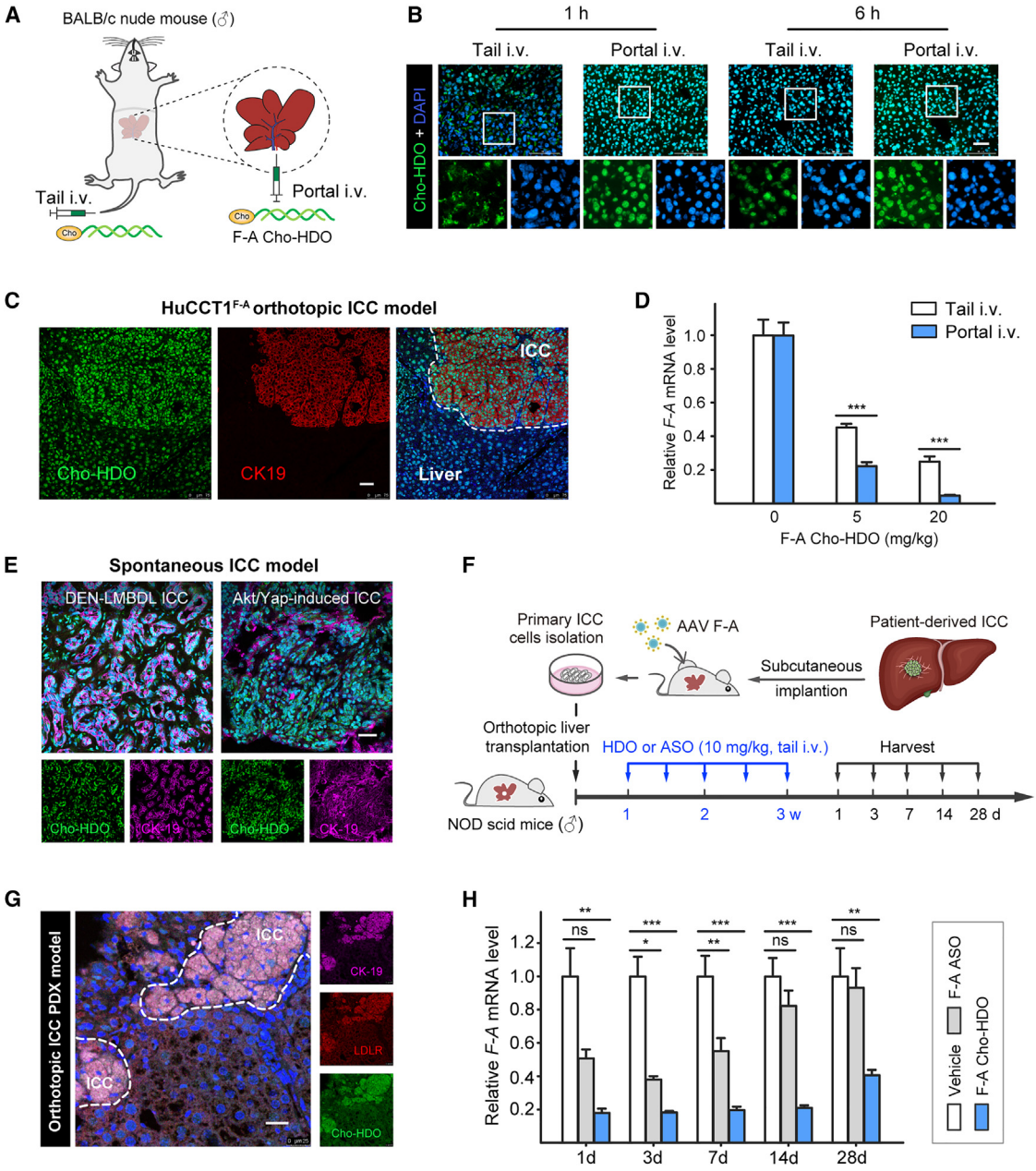

Figure 4. Biodistribution and gene silencing efficiency of F-A Cho-HDO *in vivo*

(A) Schematic illustration of the administration routes of F-A Cho-HDO in a mouse model. (B) The fluorescence of F-A Cho-HDO in the liver of mouse administrated of F-A Cho-HDO (5 mg/kg) via tail i.v. injection or portal i.v. injection. Scale bar, 50 μm. (C) The fluorescence of F-A Cho-HDO in the liver of orthotopic CDXs (HuCCT1^{F-A}) treated with F-A Cho-HDO (5 mg/kg) for 6 h through tail i.v. injection. Scale bar, 50 μm. (D) *F-A* mRNA levels of orthotopic CDXs (HuCCT1^{F-A}) treated with F-A Cho-HDO for 6 h through tail i.v. or portal i.v. injection. ***$p < 0.001$. (E) Mice with Akt/Yap-induced ICC or DEN-LMBDL-induced ICC were treated with F-A Cho-HDO (5 mg/kg) for 6 h through tail i.v. injection. F-A Cho-HDO fluorescence in mouse livers was detected using confocal fluorescence microscopy. Scale bar, 50 μm. (F) Schematic of the schedule for F-A ASO or F-A Cho-HDO treatment in the orthotopic ICC PDX mouse model. (G) Representative image of CK19, LDLR, and F-A Cho-HDO fluorescence in the orthotopic ICC PDX mouse model described in (F). Scale bar, 25 μm. (H) RT-qPCR analysis of *F-A* mRNA levels in the ICC tissues mentioned in (F). *$p < 0.05$, **$p < 0.01$, ***$p < 0.001$.

nude mice with a large dose of F-A Cho-HDO (20 mg/kg or 50 mg/kg) via tail vein injection (twice a week for 2 weeks and then once a week for another 2 weeks) and performed hematological and serum biochemical analyses to evaluate its safety. Neither dose of F-A Cho-HDO affected cardiac markers (LDH and CK) (Figure S3A). A mild elevated alkaline phosphatase (ALP), aspartate aminotransferase

(AST), and total bilirubin were found in the 50 mg/kg group and may be related to the high concentration of HDO in the liver and its immunogenicity (Figure S3B). To further evaluate the hepatic toxicity of HDO, we additionally examined mouse liver histopathology after HDO treatment, and no evidence of typical features of HDO-induced liver injury were found, such as hepatitis, necrosis, or increased apoptosis, in the mouse livers (Figure S3C). Immunogenicity is considered a side effect of nucleic acid drugs,[43,44] we also evaluated the immune response in mouse livers after HDO treatment. Neither neutrophil (Ly6G-positive) nor macrophage (F4/80-positive) infiltration was significantly increased, indicating the absence of immune-mediated injury (Figure S3D). Meanwhile, the CCK8 assay results showed that F-A Cho-HDO has no apparent effects on cell viability and the expression of WT FGFR2 of a human hepatic cell line LO2 (Figures S3E and S3F). Due to renal clearance of HDO, small increases in creatinine (CREA) and urea were also found in the 50 mg/kg group (Figure S3G). However, both doses of F-A Cho-HDO had minimal effects on the final body weight and liver/body weight ratio of mice (Figures S3H and S3I). According to our daily observation, there were no significant differences in the daily food intake, water intake, and activities of the F-A Cho-HDO-treated mice compared with mice in the vehicle group. Therefore, the delivery of F-A Cho-HDO through tail vein injection was well tolerated in mice and would be beneficial for ICC-targeted therapy.

Systemic delivery of F-A Cho-HDO reduces F-A expression and suppresses tumor progression in ICC PDX mouse models

We next tested the anti-ICC effect of F-A Cho-HDO *in vivo*. The effects of drugs used for pharmacodynamic evaluations in CDX models are usually highly dissimilar from the clinical effects due to the loss of tumor heterogeneity and the complexity of the microenvironment. Therefore, we subcutaneously transplanted a clinical ICC tissue into NOD-scid mice. Since we were unsure whether this ICC tissue harbored the F-A mutation, we performed intratumoral injection of AAV F-A to induce the expression of F-A. Subcutaneous ICC tissues exhibiting F-A expression were then implanted subcutaneously or digested into single-cell suspensions and transplanted into the livers of other NOD-scid mice to establish F-A-driven subcutaneous or orthotopic PDX models for evaluation of the anti-ICC effect of F-A Cho-HDO (Figure 5A).

In the subcutaneous PDX model, F-A Cho-HDO significantly inhibited the growth of subcutaneous ICC (Figures 5B, S3A, and S3B). Immunohistochemical (IHC) staining revealed that F-A Cho-HDO significantly reduced F-A expression, and mice treated with F-A Cho-HDO had significantly fewer Ki67-positive cells than mice in the vehicle group (Figure 5C). Previously, we demonstrated that Cho-HDO can be enriched in ICC tissue. We further evaluated the therapeutic efficacy of HDO by injecting F-A HDO or F-A Cho-HDO into mice in the orthotopic ICC PDX model through the tail vein. Compared with F-A HDO, F-A Cho-HDO more significantly attenuated the growth of orthotopic ICC PDX tumors, and this attenuation was accompanied by reductions in Ki67 and F-A expression and increases in apoptosis markers, such as cleaved-caspase 3 and cleaved-PARP (Figures 5D and 5E). In addition, the activation of FGFR2 and the downstream mediators p-FRS2, p-Akt, and p-ERK1/2 was significantly inhibited, while the levels of cleaved-caspase-3 and cleaved-PARP were markedly increased upon F-A Cho-HDO treatment (Figure 5F). Moreover, compared with that in the F-A HDO group, the survival of mice in the F-A Cho-HDO group was prolonged (Figure 5G). Similar results were observed in the orthotopic HuCCT1^{F-A} CDX model (Figures S4C–S4G). F-A Cho-HDO showed a better anti-ICC effect than F-A HDO, an effect attributed to the ability of F-A Cho-HDO to be enriched at ICC sites and accumulate to a higher concentration. In summary, F-A Cho-HDO inhibited F-A-driven ICC progression by downregulating F-A expression and blocking the downstream pro-survival pathway. This finding is expected to provide new ideas for the targeted therapy of ICC harboring FGFR2 fusion mutations.

ASNS upregulation in response to F-A Cho-HDO treatment impedes ICC growth suppression through Asn-mediated p53 repression

Despite the impressive clinical benefit of receptor tyrosine kinase inhibitors (TKIs), the development of therapeutic resistance remains a challenge.[45] Tumors usually evade the sanction of targeted therapy via various mechanisms, leading to failure of targeted therapy. FGFR kinase inhibitors (including pemigatinib) are no exception, and patients acquire resistance due to acquisition of amino acid mutations or activation of alternative pathways.[46] In this situation, combination therapy is often required to produce better therapeutic effects.

Herein, we performed RNA sequencing (RNA-seq) analysis on F-A-overexpressing ICC primary cell lines treated with F-A Cho-HDO to identify activated bypass pathways. A series of genes was significantly upregulated or downregulated following F-A Cho-HDO treatment (Figure 6A). Gene Ontology (GO) enrichment analysis revealed that the upregulated genes were involved in cell cycle regulation, as terms such as positive regulation of mitotic cell cycle, cell division, mitotic cell cycle, and chromosome segregation were enriched in these genes (Figure 6B). Among these genes, *ASNS*, with the most significant difference, has been reported to participate in the regulation of the G1 phase through ts11[47] or promote cell cycle progression by inhibiting p53 through Asn.[48] Previously, we observed that F-A Cho-HDO did not significantly suppress the cell cycle in F-A-positive ICC cells. Accordingly, we speculated that F-A inhibition by F-A Cho-HDO leads to upregulation of ASNS and promotes cell cycle progression, which largely neutralizes the anti-ICC effect of F-A Cho-HDO. To verify our hypothesis, we first confirmed whether treatment with F-A Cho-HDO induces upregulation of ASNS. Both in patient-derived primary ICC cells and in the HuCCT1^{F-A} cell line, *ASNS* mRNA and protein levels were markedly increased after F-A Cho-HDO treatment (Figures 6C, S5A, and S5B). Does upregulation of ASNS promote cell cycle progression in ICC cells? Considering the limited time available for culturing primary ICC cells *in vitro*, we conducted subsequent experiments on the HuCCT1^{F-A} ICC cell line. A significant increase in the percentage of cells in G1 phase was observed in HuCCT1^{F-A} cells after treatment with the combination of F-A Cho-HDO and siASNS compared with F-A Cho-HDO monotherapy

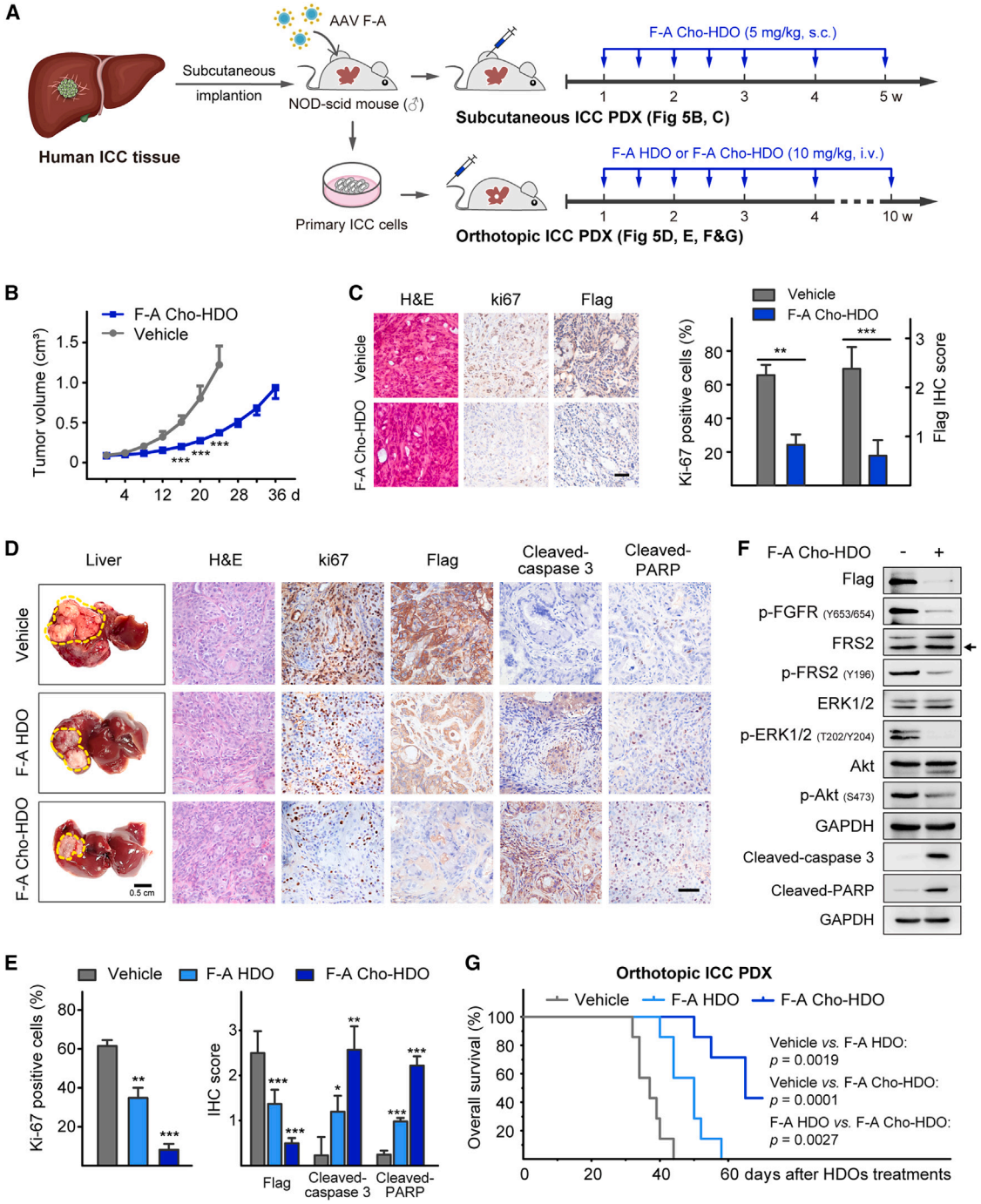

Figure 5. Anti-ICC effects of F-A Cho-HDO in ICC PDX mouse models

(A) Schematic of the establishment of the subcutaneous and orthotopic ICC PDX models. (B) The volumes of subcutaneous ICC PDX tumors were measured every 4 days (n = 7). ***p < 0.001 vs. vehicle. (C) Representative images of H&E staining and IHC staining of Ki67 and Flag (F-A) in subcutaneous ICC PDXs and their statistical analysis. Scale bar, 50 μm. **p < 0.01, ***p < 0.001. (D) Representative images of tumor morphology, H&E staining, and IHC staining of indicated proteins in orthotopic ICC PDXs. Scale bar, 50 μm. (E) Statistical analysis of (D), *p < 0.05, **p < 0.01, ***p < 0.001 vs. vehicle. (F) Expression of indicated proteins in orthotopic ICC PDXs were measured by western blotting. (G) Kaplan-Meier curves showing the overall survival of mice with indicated treatments in the orthotopic ICC PDX model.

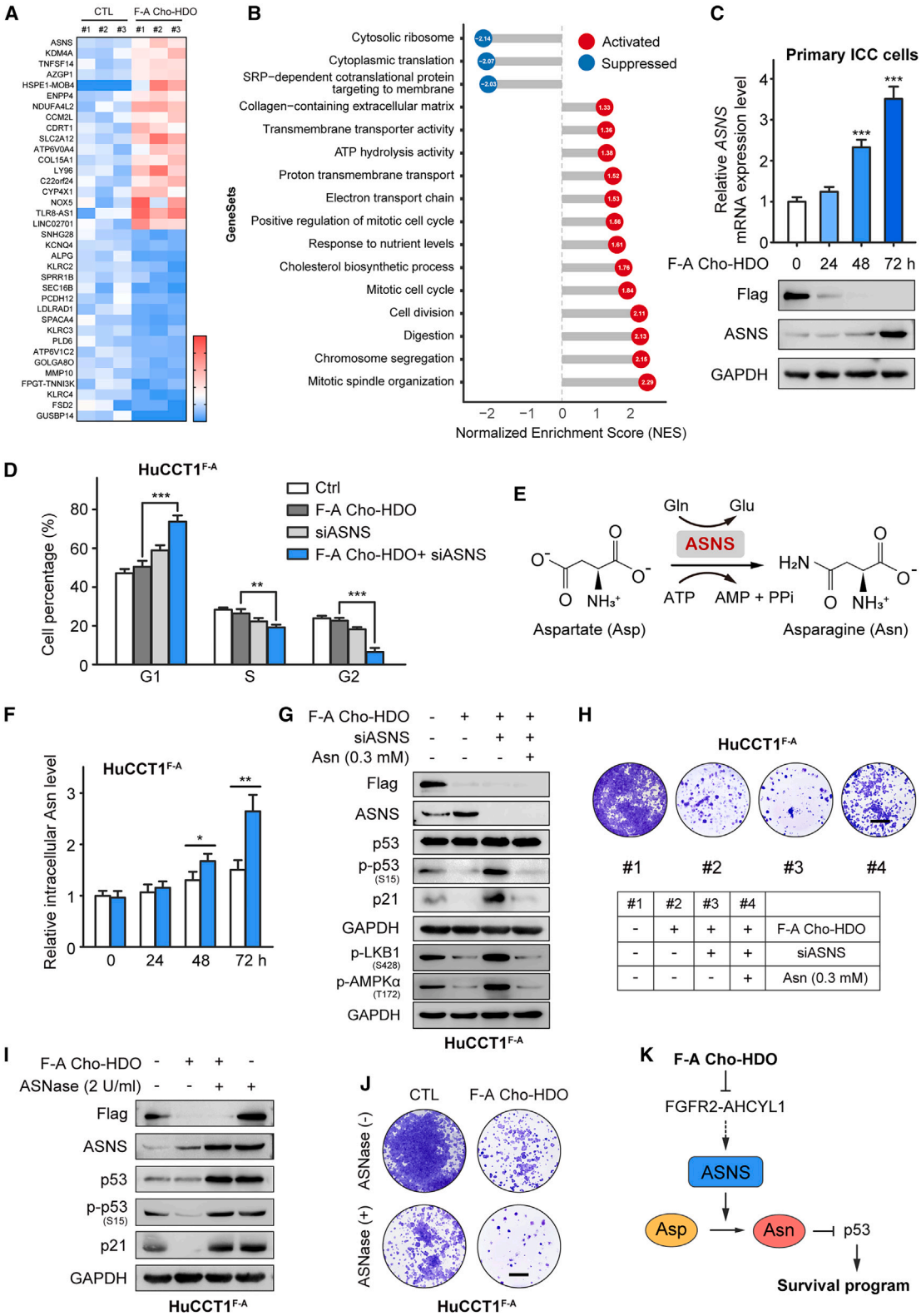

(legend on next page)

(Figure 6D), indicating that F-A Cho-HDO treatment promotes cell cycle progression by upregulating ASNS. ASNS is localized predominantly in the cytosol and catalyzes the conversion of aspartate (Asp) into Asn (Figure 6E). Indeed, the intracellular Asn level in HuCCT1^{F-A} cells was increased after F-A Cho-HDO treatment (Figure 6F). It has been reported that Asn can inhibit the phosphorylation of liver kinase B1 (LKB1) through direct interaction, and then inhibits the phosphorylation of AMPK that activates p53 through phosphorylation. Therefore, the consequence is that Asn mitigates p53-dependent cell cycle arrest,[48] but whether the promotion of cell cycle progression by ASNS is related to the increase in the intracellular Asn level remains unknown. To verify the above findings, we also evaluated the phosphorylation of LKB1, AMPK, and p53 in HuCCT1^{F-A} cells after F-A HDO treatment. Upon F-A HDO treatment, the expression of ASNS was upregulated, while the phosphorylation of LKB1, AMPK and p53, and p21 expression were significantly reduced (Figure 6G). However, the levels of p21, phosphorylated LKB1, AMPK, and p53 were restored after knockdown of *ASNS*, and these processes were reversed by exogenous supplementation with Asn (Figure 6G), suggesting that ASNS may promote cell cycle progression by suppressing p53 through enhancing Asn synthesis. Furthermore, the F-A Cho-HDO-mediated inhibition of HuCCT1^{F-A} cell proliferation was further enhanced after *ASNS* knockdown, but the addition of Asn abrogated this effect (Figure 6H). Similar results were obtained using L-albizziine (L-Alb), a competitive inhibitor of ASNS that decreases the intracellular Asn level. The addition of L-Alb reactivated p53 and p21 after their suppression by F-A Cho-HDO, while Asn addition abolished this effect (Figure S5C). ASNase, a first-line therapy for childhood acute lymphoblastic leukemia, exerted antitumor effects by degrading Asn.[49,50] Asn depletion by ASNase treatment reactivated p53 and restored p21 expression, thereby enhancing the inhibition of HuCCT1^{F-A} cell proliferation induced by F-A Cho-HDO treatment (Figures 6I, 6J, and S5D). The data presented above suggested that F-A inhibition by F-A Cho-HDO leads to upregulation of ASNS and increases Asn synthesis, resulting in inhibition of p53, which promotes cell survival and partially weakens the therapeutic effects of F-A Cho-HDO (Figures 6K and S5E).

Enhanced *ASNS* transcription activity following F-A Cho-HDO treatment is dependent on EGFR/STAT1 signaling

We next investigated the mechanisms underlying the increased ASNS protein level after F-A Cho-HDO treatment. Since the mRNA level of *ASNS* was increased, the potential transcription factors of *ASNS* were predicted using the UCSC Genome Browser database (http://genome.ucsc.edu). The most overrepresented potential *ASNS* transcription factors included those in the ZNF, KLF, CTCF, and STAT families (minimum score >500). Our previous RNA-seq analysis showed that the expression level of STAT1 was significantly increased after F-A Cho-HDO treatment. To determine whether STAT1 is involved in ASNS transcription, we used the JASPAR database (http://jaspar.genereg.net/) for analysis, which revealed 10 potential STAT1 binding sites in the promoter region of ASNS (Table S1). The top three potential binding sites were generally characterized by higher motif scores that matched the STAT1 consensus motif; thus, we designed three pairs of chromatin immunoprecipitation (ChIP) primers to analyze the interaction of STAT1 with the *ASNS* promoter region (Figure 7A). ChIP-qPCR analysis showed that the ASNS promoter fragments were significantly amplified from the F-A Cho-HDO-treated HuCCT1^{F-A} cell sample (Figure 7B), indicating that STAT1 directly promotes ASNS transcription. Furthermore, the upregulation of ASNS and the increase in the intracellular Asn level induced by F-A Cho-HDO were abrogated by STAT1 siRNA transfection (Figures 7C and 7D). The decreases in p53 phosphorylation and p21 expression caused by the increased intracellular Asn level were also reversed by STAT1 siRNA transfection (Figure 7C), accompanied by a further increase in G1 arrest (Figure 7E). These results indicate that STAT1 is a potent transcription factor that is necessary for F-A Cho-HDO-induced upregulation of ASNS.

However, how does F-A Cho-HDO lead to upregulation of STAT1? Previous studies have shown that activation of alternative bypass signaling pathways, such as the RAS-MAPK, ERK, PI3K-Akt, or other RTK (EGFR, ERBB2, ERBB3, and MET) pathways, induces resistance to FGFR kinase inhibitors.[19] Among the molecules in these alternative bypass signaling pathways, F-A Cho-HDO effectively inhibited the phosphorylation of ERK1/2 and Akt (Figures 1E and 5F), and the phosphorylation of MET, ERBB2, and ERBB3 was not affected (data not shown), whereas F-A Cho-HDO stimulated noticeable phosphorylation of EGFR (Figure S6A). Thus, we speculated that inhibition of F-A stimulates alternative EGFR activation, leading to upregulation of STAT1. Indeed, with continued F-A Cho-HDO treatment, the phosphorylation level of EGFR and protein level of STAT1 gradually increased in F-A-positive ICC cells, in direct contrast to F-A downregulation (Figure 7F). However, when EGFR was inhibited by treatment with gefitinib (a specific EGFR inhibitor), the upregulation of STAT1 and ASNS, as well as the increase in the intracellular Asn

Figure 6. ASNS upregulation upon F-A Cho-HDO treatment enhanced intracellular Asn synthesis, promoting ICC cell survival by inhibiting p53

(A) Significantly upregulated or downregulated genes in primary ICC cells upon F-A Cho-HDO treatment are shown in the heatmap. (B) GO enrichment analysis of significantly differentially expressed genes in primary ICC cells upon F-A Cho-HDO treatment. (C) The *ASNS* mRNA and protein levels in HuCCT1^{F-A} cells treated with F-A Cho-HDO (200 nM) for 24, 48, and 72 h were measured by RT-qPCR and western blotting. ***$p < 0.001$ vs. 0 h. (D) The distribution of cell cycle phase in HuCCT1^{F-A} cells treated with F-A Cho-HDO (200 nM) in the presence or absence of siASNS (400 nM) for 72 h. **$p < 0.01$, ***$p < 0.001$. (E) Schematic diagram describing the reaction catalyzed by ASNS. (F) Qualification of relative intracellular Asn levels in HuCCT1^{F-A} cells treated with F-A Cho-HDO (200 nM) for the indicated times. *$p < 0.05$, **$p < 0.01$. (G and H) HuCCT1^{F-A} cells transfected with F-A Cho-HDO in the presence or absence of siASNS (400 nM) were cultured with or without Asn (0.3 mM) for 72 h. The indicated protein levels were measured by western blotting (G), and cell proliferation was measured by a colony formation assay (H). Scale bar, 1 cm. (I and J) HuCCT1^{F-A} cells transfected with F-A Cho-HDO were treated with or without ASNase (2 U/mL) for 72 h. The indicated protein levels were measured by western blotting (I), and cell proliferation was measured by a colony formation assay (J). Scale bar, 1 cm. (K) Model showing the cellular survival program orchestrated by F-A Cho-HDO-induced upregulation of ASNS.

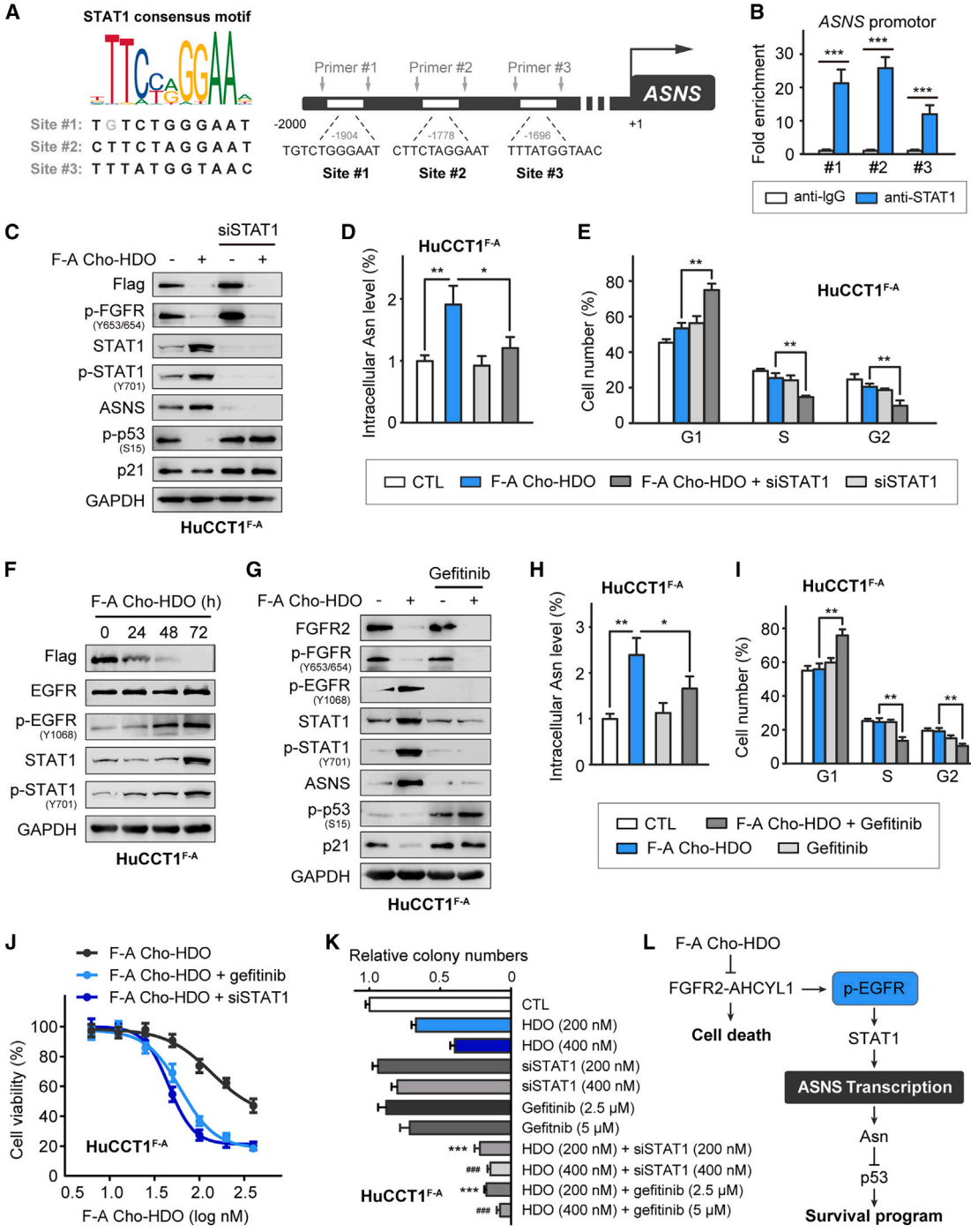

Figure 7. EGFR bypass activation after F-A Cho-HDO treatment promoted STAT1-mediated *ASNS* transcription and Asn synthesis in ICC cells

(A) Sequence logo of the binding specificity of STAT1 predicted using the JASPAR database (left). Diagram of potential STAT1-binding sites in the *ASNS* promoter region (right). (B) ChIP-qPCR analysis of STAT1 occupancy of the *ASNS* promoter in HuCCT1^{F-A} cells treated with F-A Cho-HDO (200 nM) for 72 h. ***$p < 0.001$. (C–E) HuCCT1^{F-A} cells were transfected with F-A Cho-HDO (200 nM) in the presence or absence of siSTAT1 (400 nM) for 72 h, and the indicated protein levels (C), relative intracellular Asn levels (D) and cell cycle distribution (E) were measured, *$p < 0.05$, **$p < 0.01$. (F) Western blotting analysis of the indicated proteins in HuCCT1^{F-A} cells upon F-A Cho-HDO (200 nM) treatment. (G–I) HuCCT1^{F-A} cells were transfected with F-A Cho-HDO (200 nM) in the presence or absence of gefitinib (5 μM) for 72 h, and the indicated protein levels (G),

(legend continued on next page)

level induced by F-A Cho-HDO, were significantly inhibited, and the decreases in p53 phosphorylation and p21 expression were also reversed (Figures 7G and 7H). Cell cycle analysis showed that the combination of gefitinib and F-A Cho-HDO further increased G1 arrest (Figure 7I). In addition, the combination of F-A Cho-HDO and either STAT1 siRNA or gefitinib had greater anti-ICC effects than F-A Cho-HDO monotherapy *in vitro* (Figures 7J, 7K, S6C, and S6D). These data indicate that F-A downregulation by F-A Cho-HDO leads to bypass activation of EGFR signaling, accompanied by STAT1 upregulation, which increases *ASNS* transcription and intracellular Asn synthesis, thereby activating the survival program by inhibiting p53 (Figure 7L). Blocking this alternative activation of EGFR with gefitinib can enhance the therapeutic effect of F-A Cho-HDO *in vitro*.

A previous study identified signaling feedback via the EGFR pathway as a major mediator of adaptive resistance to FGFR kinase inhibition by infigratinib treatment in a series of patient-derived ICC models.[51] To investigate whether F-A HDO-induced bypass activation of the EGFR-STAT1-ASNS axis also occurs upon pemigatinib treatment, we treated ICC cells with increasing concentrations of pemigatinib and found that the protein levels of p-EGFR (Y1086), STAT1, and ASNS were gradually increased, accompanied by an increase in the intracellular Asn level (Figures S6E and S6F). In addition, EGFR inhibition by gefitinib treatment or asparagine deprivation by asparaginase treatment increased the sensitivity of ICC cells to pemigatinib (Figure S6G). These results suggest that activation of the EGFR-STAT1-ASNS pathway is a common event following inhibition of FGFR2 fusion expression in ICC via either inhibition of kinase activity or reduction of protein expression.

ASNase or gefitinib enhances therapeutic effect of F-A Cho-HDO in F-A-positive ICC PDX models

We previously found that Asn promoted ICC proliferation by suppressing p53 and led to attenuation of the anti-ICC effect of F-A Cho-HDO *in vitro*; moreover, we determined that simultaneous inhibition of F-A and ASNS could achieve a better anti-ICC effect than inhibition of F-A alone. To further validate the efficacy of this combination therapy *in vivo*, subcutaneous and orthotopic xenografts were established in NOD-scid mice using F-A-positive human ICC tissue through intratumoral injection of AAV F-A (described in Figure 5A), and the combination therapy was administered according to the flow chart in Figure 8A. The anti-ICC effect of F-A Cho-HDO combined with either gefitinib or ASNase in the subcutaneous ICC PDX model was more significant than that of F-A Cho-HDO alone (Figures 8B, 8C, and S7A). Gefitinib blocked the increases in the STAT1, p-STAT1, and ASNS protein levels as well as the increase in the intratumoral Asn level induced by F-A Cho-HDO, and reversed the decreases in the p-p53 and p21 levels caused by elevated Asn level in subcutaneous PDXs (Figures 8D and 8F). In addition, depletion of Asn by ASNase treatment led to reversal of the decreases in p-p53 and p21 (Figures 8D and 8F). The above results were consistent with those obtained *in vitro*, further verifying that the combination treatment more effectively suppressed F-A-positive ICC. We next initiated injection of F-A Cho-HDO combined with administration of ASNase or gefitinib after the establishment of orthotopic ICC PDXs (Figure 8A). Compared with that in mice treated with F-A Cho-HDO alone, more significant inhibition of orthotopic ICC PDX growth was observed in both combination treatment groups, accompanied by a significant reduction in the number of Ki67-positive cells (Figures 8E and S7B). IHC staining revealed that compared with F-A Cho-HDO alone, the combination of F-A Cho-HDO and gefitinib significantly decreased the protein levels of p-EGFR, STAT1, ASNS, and the intratumoral Asn level (Figures 8E, 8F, and S7C), since ASNase depleted both endogenous and exogenous Asn, but gefitinib only impaired de novo synthesized Asn (endogenous Asn) through downregulation of ASNS via inhibition of EGFR. Therefore, although ASNase treatment did not decrease the protein levels of p-EGFR, STAT1, and ASNS (Figure 8E), it reduced the intratumoral Asn level more significantly than did gefitinib (Figure 8F), thereby exerting a more potent anti-ICC effect. These data further demonstrated that Asn depletion enhanced the anti-ICC effect of F-A Cho-HDO *in vivo*. In addition, the combined therapy resulted in longer survival times in mice bearing orthotopic ICC PDXs than did F-A Cho-HDO treatment alone (Figure 8G). Taken together, these results indicated that the combination of F-A Cho-HDO with either of two clinical medications (gefitinib or ASNase) effectively inhibited ICC progression driven by F-A in this mouse model. This combination therapy may provide new ideas for the treatment of ICC harboring FGFR2 fusion mutations.

DISCUSSION

Tumorigenic FGFR2 fusion mutations are frequently identified in ICC,[52] and targeting FGFR2 fusion mutations through genetic engineering is a precise therapeutic strategy.[53] However, efficient gene silencing using therapeutic oligonucleotides remains challenging in ICC cells since these cells are highly resistant to transfection owing to their thin cell membrane, limited endocytosis, and relatively low cell surface protein expression.[54] Prof. Takanori Yokota developed Cho-HDO, a new efficient nucleic acid drug, to target specific pathogenic genes in the liver or brain with low immunogenicity and cytotoxicity.[25] The effect of Cho-HDO on ICC cells and tumors harboring an FGFR2 fusion mutation was investigated in this study. We found high expression of LDLR in ICC, thus identifying an effective strategy for the targeted delivery of nucleic acid drugs. In addition, we identified an alternative mechanism for resistance to FGFR2 fusion inhibitors: bypass activation of EGFR leads to upregulation of STAT1, which promotes the transcription of ASNS and then increases

relative intracellular Asn level (H), and cell cycle distribution (I) were quantified. *$p < 0.05$, **$p < 0.01$. (J) The cell viability of HuCCT1^{F-A} cells treated with F-A Cho-HDO in the presence or absence of siSTAT1 (400 nM) or gefitinib (5 μM) for 72 h was measured by a CCK-8 assay. (K) Relative colony-forming ability of HuCCT1^{F-A} cells transfected with F-A Cho-HDO in the presence or absence of siSTAT1 or gefitinib. ***$p < 0.001$ vs. HDO (200 nM), ###$p < 0.001$ vs. HDO (400 nM). (L) Model showing the cellular survival program orchestrated by EGFR bypass signaling activation upon F-A Cho-HDO treatment.

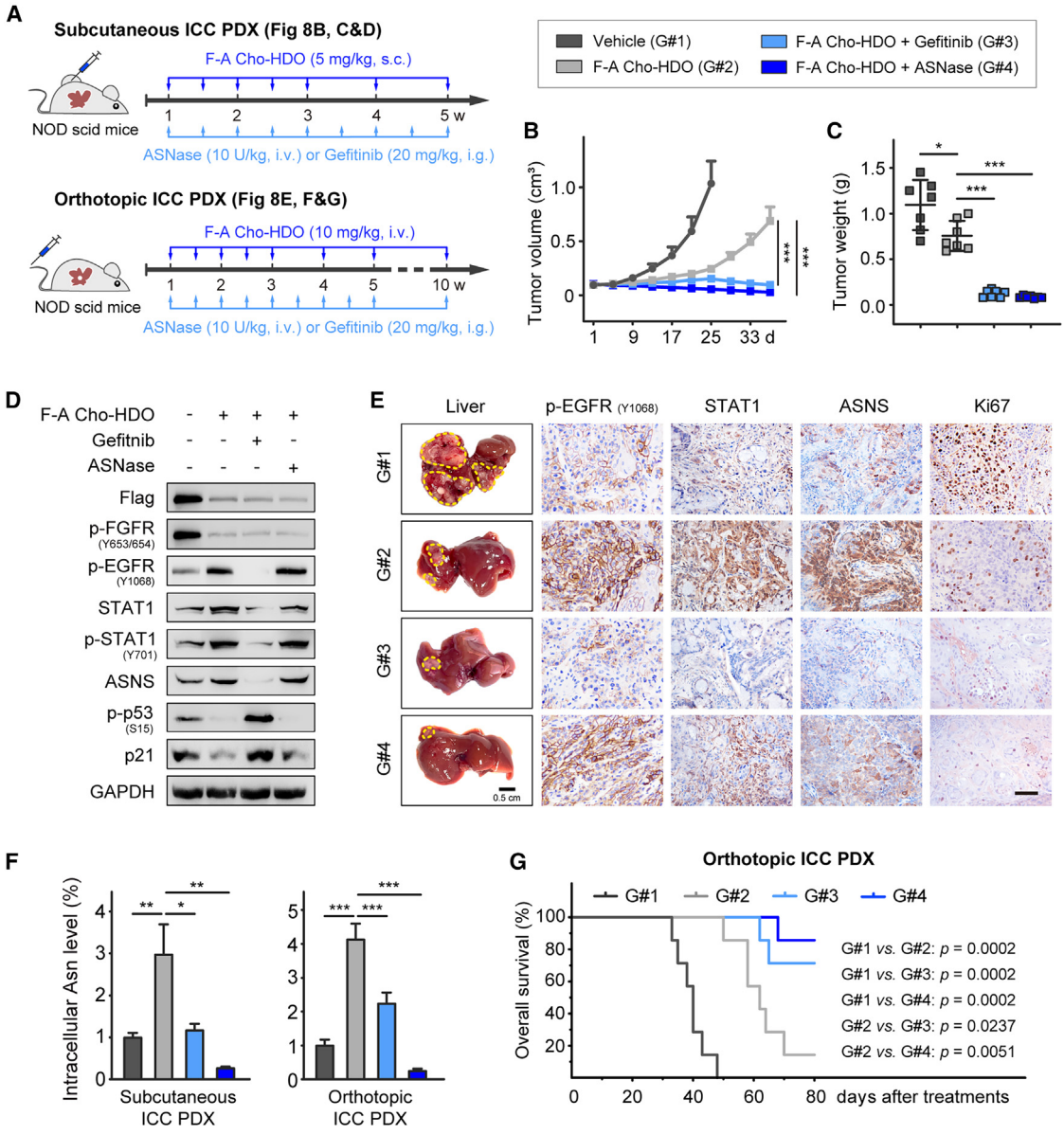

Figure 8. F-A Cho-HDO in combination with ASNase or gefitinib significantly impaired F-A-driven ICC progression

(A) Design of the combination therapy study. (B) Tumor volume curves of mice in the subcutaneous ICC PDX model (n = 7). ***p < 0.001. (C) Final tumor weights of mice in the subcutaneous ICC PDX model (n = 7). *p < 0.05, ***p < 0.001. (D) The indicated protein levels in subcutaneous ICC PDXs were measured by western blotting. (E) Representative images of livers harboring ICC PDX tumors and IHC staining of indicated proteins in orthotopic ICC PDX tumors. Scale bar, 100 μm. (F) Relative intracellular Asn levels in subcutaneous ICC PDX and orthotopic ICC PDX samples with indicated treatments (n = 7). *p < 0.05, **p < 0.01, ***p < 0.001. (G) Kaplan-Meier survival curves of mice with indicated treatments in the orthotopic ICC PDX model.

intracellular Asn synthesis, which contributes to reducing the efficiency of F-A Cho-HDO via suppression of p53. Encouragingly, a significant synergistic effect was observed after treatment with F-A Cho-HDO combined with either of two clinical drugs (gefitinib and ASNase). This study provides a rationale for the clinical evaluation of strategies cotargeting FGFR2 fusions and Asn metabolism pathways for cancer therapy.

In this study, we chose a classical FGFR2 fusion, F-A, and designed a Cho-HDO targeting the chimeric region that prevents unwanted off-target effects on WT *FGFR2* or WT *AHCYL1*. Self-deliverable and chemically modified ASOs have exhibited high efficiency and specificity for target gene suppression.[55] HDOs display greater potency and stability than the parental ASOs *in vivo* and *in vitro* and may undergo clinical translation as the next generation of more efficient

nucleic acid drugs.[56] However, there are still challenges in the development of the delivery platform. It has been reported that HDOs are stabilized in serum by conjugation with serum lipoproteins, thereby enhancing their productive delivery to the liver[57] and providing a new therapeutic approach for liver diseases. However, few studies have investigated the delivery of Cho-HDOs to ICC tissues. In this study, we found that LDLR is highly expressed in ICC cells and tissues, leading to specific accumulation of Cho-HDO in ICC. Our data showed that Cho-HDO can associate with LDL in plasma and enter ICC cells through LDLR-mediated endocytosis. Considering the heterogeneity of LDLR expression in ICC, it may be beneficial to preevaluate ICC patients based on functional LDLR receptor expression, thereby ensuring the clinical efficacy of Cho-conjugated HDOs. Clinically, PVC improves the survival outcomes of people with advanced HCC and ICC. Injection of Cho-HDO through the portal vein can rapidly increase its concentration at the lesion site with low concentrations in other organs. However, administration through the portal vein is transient at the detriment of the mouse. Therefore, we administered Cho-HDO through the tail vein in this study to simulate clinical intravenous infusion. We found that Cho-HDO can be effectively enriched in ICC sites when administered through tail vein injection. Given the above advantages, Cho-HDO may be a practical technique for the treatment of ICC patients.

Acquired resistance is a major problem limiting the clinical efficacy of targeted therapies.[58] In our study, a high basal level of ASNS was observed after F-A Cho-HDO treatment. ASNS, an enzyme critical for endogenous Asn synthesis and cell proliferation,[59] has been shown to play an important role in promoting cell cycle progression.[60,61] We found that disruption of ASNS expression or activity leads to p53-dependent cell cycle arrest and then promotes ICC cell death by decreasing Asn synthesis. Despite the accumulating knowledge regarding the biological function of ASNS, little is known about how its expression is controlled at the transcriptional level. Here, we identified STAT1 as a transcription factor of *ASNS*, as evidenced by the binding of STAT1 to the ASNS promoter. This finding revealed that loss of STAT1 expression decreases the Asn level, leading to cell cycle arrest followed by proliferation inhibition. However, how F-A Cho-HDO leads to the upregulation of STAT1 remains unknown. The crosstalk between FGFR and other RTKs elicits notorious resistance to FGFR-targeted therapies.[51] Our results support this idea and provide an explanation for why F-A Cho-HDO-mediated inhibition leads to STAT1 upregulation. To further investigate bypass signaling axes mediated by Cho-HDO, classical tyrosine kinases (including ERBB2, MET, and EGFR) were evaluated. Among molecules in these pathways, EGFR was activated, and inhibition of EGFR by gefitinib treatment reduced the expression of STAT1 and ASNS. Targeting FGFR2 fusion mutations with HDOs can lead to bypass signaling activation (indeed, it is inevitable, based on the characteristics of cancer). Fortunately, EGFR and ASNS are actionable tumor targets that can be targeted by clinical drugs. We demonstrated that the combination of F-A Cho-HDO with ASNase or gefitinib can result in better outcomes than F-A Cho-HDO monotherapy in murine ICC PDX models. Notably, the effect of F-A Cho-HDO + ASNase was better than that of F-A Cho-HDO + gefitinib, possibly because ASNase treatment results in deprivation of both endogenous and exogenous Asn. However, gefitinib inhibits the expression of ASNS by inhibiting EGFR, which reduces the level of only endogenous Asn. Therefore, targeting the Asn metabolism pathway may constitute a potent strategy to sensitize tumors to FGFR inhibitors.

Despite the aforementioned benefits, some limitations need to be highlighted. LDLR is highly expressed on ICC cells, but it is also expressed on hepatocytes. Therefore, F-A Cho-HDO can also enter hepatocytes. Fortunately, F-A Cho-HDO was designed to target the chimeric segment of F-A, with no effects on WT *FGFR2* and WT *AHCYL1* in ICC cells. Moreover, FGFR2 fusion mutations occur only in ICC cells, not in normal hepatocytes. Although F-A Cho-HDO does not target any sequence in normal tissues, its effect on the function of hepatocytes needs further exploration. In addition, treatments such as targeted therapies are increasingly being tailored to the key genetic mutations that drive cancers. As mentioned above, acquired drug resistance remains a concern. The potential "seeds" of resistance-alternative activation decrease the efficacy of targeted treatments. Identifying the mechanisms through which cancer cells undergo "rewiring" of their circuitry through bypass activation to evade treatment effects may be essential for the development of more successful combination approaches. In this study, we found that F-A Cho-HDO induces ASNS upregulation. Abrogation of FGFR2 fusion and ASNS expression further blocked tumor growth, providing a rationale for this combination therapy. However, whether other bypass activation mechanisms exist that reduce the efficacy of F-A Cho-HDO remains unclear. Through RNA-seq analysis, we also identified other bypass signaling drivers that may promote ICC survival, such as *KDM4A*, *ATP6V0A4*, *ENPP4*, *CCM2L*, and *COL15A1*. Some of those genes (*ATP6V0A4*) activate the electron transport chain and ultimately result in the generation of ATP, which maintains drug resistance and promotes tumor growth. Similarly, other genes (such as *CCM2L* and *COL15A1*) may increase the synthesis of collagen, which is the main component of the extracellular matrix and plays a role in regulating tumor metastasis.[62] These results elucidated the reason for the limited efficacy of F-A Cho-HDO as a single agent, i.e., reciprocal activation of bypass pathways. These issues as well as the precise mechanisms of other alternative pathways may be investigated in future studies.

Taken together, our findings showed that LDLR, an efficient endocytic surface receptor, is highly expressed in human and murine ICC. This finding is expected to provide new ideas for the delivery of Cho-HDO to ICC sites. We employed a murine ICC PDX model with F-A expression to functionally validate Cho-HDO as a disabler of FGFR2 fusions. Our studies demonstrated that the adaptation to F-A Cho-HDO is dependent on EGFR/STAT1/ASNS signaling. Thus, combination therapy employing F-A Cho-HDO and Asn deprivation is anticipated to elicit better outcomes. To that end, our study ushers in a new era in the use of Cho-HDO for targeted therapy

of ICC and provides new insights into clinical FGFR2 inhibitor resistance and combination strategies in ICC therapy.

MATERIALS AND METHODS

Reagents and antibodies

Pitstop 2, DEN, glycine, sodium pyruvate, gentamicin, and L-Asparagine were purchased from Sigma-Aldrich (St. Louis, MO, USA). L-Albizziine, gefitinib, and pemigatinib were obtained from Selleck Chemicals (Texas, USA). L-Asparaginase was purchased from ProSpec Bio (Israel). Lipofectamine 3000 transfection reagent, 4′,6-diamidino-2-phenylindole (DAPI) and Triton X-100 were obtained from Thermo Fisher Scientific (Waltham, MA, USA). Puromycin was purchased from Solarbio Science & Technology Co., Ltd. (Beijing, China). Actin-Tracker Red-594 was obtained from Beyotime Biotechnology (Shanghai, China). Matrigel Matrix was purchased from Corning Life Sciences (Corning, NY, USA). All other reagents were purchased from Sigma-Aldrich (St. Louis, MO, USA). All information on antibodies used in this study is listed in Table S2.

Plasmids, lentivirus, and adeno-associated virus construction and transfection

The *FGFR2-AHCYL1* plasmid contains a C-terminal FLAG tag (Flag F-A) that was constructed by Genechem Co., Ltd. (Shanghai, China). The constructs were generated by cloning *FGFR2-AHCYL1* cDNA into the GV492 vector (Ubi-MCS-3FLAG-CBh-gcGFP-IRES-puromycin). The plasmids encoding LDLR were gifts from Marvin Bentley Lab (Addgene plasmid # 162717). For transient transfection, plasmids were transiently transfected into ICC cells using Lipofectamine 3000 reagents according to the manufacturer's instructions. pT3-myr-AKT-HA (Addgene plasmid # 31789) and pT3-EF1a-YapS127A (Addgene plasmid # 46049) were gifts from Dr. Xin Chen. Lentivirus containing *FGFR2-AHCYL1* fusion plasmid and the corresponding vector GV492 were constructed by Genechem Co., Ltd. ICC cell lines, RBE, HuCCT1, and HCCC-9810 were transfected with the FGFR2-AHCYL1 lentivirus (multiplicity of infection (MOI)) according to the manufacturer's instructions. The stable transfected RBE^{Vector}, RBE^{F-A}, $HuCCT1^{Vector}$, $HuCCT1^{F-A}$, $HCC\text{-}9810^{Vector}$, and $HCC\text{-}9810^{F-A}$ were selected under the pressure of 2 μg/mL of puromycin for 1–2 weeks. AAV9 expressing *FGFR2-AHCYL1* (rAAV-CMV-FGFR2-AHCYL1-3Flag-WPREs, AAV F-A) and rAAV-CMV-EGFP-WPRE-Hgh-pA (AAV CTL) were constructed and packaged by BrainVTA Co., Ltd. (Wuhan, China).

HDO, ASO, and siRNA synthesis and transfection

The chemical structure of HDO is shown in Figures 1B and 1F. FAM fluorophores were covalently bound to the 5′ ends of DNA/LNA gapmers. For Cho-HDO, cholesterol was covalently bound to the 5′ ends of cRNAs. HDO, Cho-HDO, and ASO used in this study were synthesized by Tsingke Biotechnology Co., Ltd. (Beijing, China). siRNA was designed and synthesized by IGE Biotechnology Co., Ltd. (Guangzhou, China). Cells were transfected with ASO, HDO, or siRNA using Lipofectamine 3000 reagents according to the manufacturer's instructions. Detailed sequence information of ASO, HDO, and siRNA used in this study were shown in supporting information Table S3.

Cell lines and cell culture

Human ICC cell lines (RBE, HCCC-9810) and extrahepatic cholangiocarcinoma (ECC) cell line TFK1 were purchased from Lvyuan Bode Biotechnology Co., Ltd. (Beijing, China). The human ICC cell line HuCCT1 was purchased from Suyan Biotechnology Co., Ltd. (Guangzhou, China). Human intrahepatic biliary epithelial cells HIBEpiC and the ECC cell line QBC939 were purchased from Zhenke Biotechnology Co., Ltd. (Shenzhen, China). Cells were identified by polymorphic short tandem repeat profiling and tested to exclude mycoplasma contamination every month. All cell lines were cultured in RPMI-1640 medium (Gibco, NY, USA) supplemented with 10% fetal bovine serum (FBS) (Excell Bio, Shanghai, China) and 1% penicillin/streptomycin (Thermo Fisher Scientific) and fostered in a humidified atmosphere of 5% CO_2.

Cell proliferation assay

For CCK8 assay, cells were seeded into 96-well plates at a density of 3,000 cells/well. After indicated treatment, cell viability was examined using a CCK8 kit (APExBIO, Houston, TX, USA) according to the manufacturer's instructions. Absorbance was measured using an iMark Microplate Absorbance Reader (Bio-Rad, Hercules, CA, USA) at 450 nm. For colony formation assay, cells (about 500) were seeded in each well of six-well plates, grown in complete medium with indicated treatments and further cultured for another 14 days. Finally, cells were fixed in methanol, washed with PBS, and stained with 0.5% crystal violet (Beyotime Biotechnology, Shanghai, China).

Combination index calculation for combination drug-treatment

After drug combination treatment, the combination index (CI) of F-A Cho-HDO with siSTAT1 or gefitinib were calculated using the Compusyn software (CompuSyn, Paramus, NJ, USA) based on the Chou-Talalay method (1984). The resulting CI theorem of Chou-Talalay described the quantitative definition for additive effect (CI = 1), synergism (CI < 1), and antagonism (CI > 1) in drug combinations.[63]

Sphere formation assay

The sphere formation assay was performed based on an ultra-low attachment culture method. Briefly, cells were seeded in 96-well ultra-low attachment plates (Corning, New York, NY, USA) in DMEM/F12 medium (Gibco, NY, USA) supplemented with 1× B27 (Thermo Fisher Scientific), 20 ng/mL of basic fibroblast growth factor (bFGF) (Thermo Fisher Scientific), and 20 ng/mL of EGF (Thermo Fisher Scientific). Templates were incubated at 37°C in a humidified atmosphere of 5% CO_2, followed by indicated treatments.

Cell migration assay

Cell migration ability was assayed using *in vitro* cell-scratch migration assay and transwell migration assay. For cell-scratch migration assays, cells were grown to full confluency in six-well plates and starved of serum overnight. Scratches were introduced using a 200-μL pipette

tip. Cells were then treated with indicated treatments. Images of the scratch were captured using an Olympus IX51 inverted microscope (Tokyo, Japan) at 0 h and every 12 h until the scratch was healed. The percentage of scratch healed was determined using ImageJ software. For transwell migration assays, transwell chambers were plated with 6×10^4 cells suspended in 200 μL of serum-free medium and 700 μL of complete medium was placed in the lower chambers. After indicated treatments, non-migrated cells were wiped away from the filter with a cotton swab and the migrated cells were fixed with 4% paraformaldehyde and stained with DAPI for 10 min, after which the migrated cells were counted manually under a Leica DMi8 fluorescence microscope (Leica, Wetzlar, Germany).

Cell apoptosis analysis

Flow cytometric experiment was performed using the cell apoptosis staining kit (MultiSciences Biotech Co., Ltd., Shanghai, China) based on the manufacture's instruction. The ICC cells were collected, stained, and subjected to ACEA flow cytometric analysis (ACEA Biosciences Inc., San Diego, CA, USA). The proportion (percentage) of cell apoptosis (early apoptosis rate + late apoptosis rate) was analyzed using the ACEA NovoExpress software (ACEA Biosciences Inc.).

Cell cycle analysis

Cell cycle analysis was carried out using a cell cycle staining kit (MultiSciences Biotech Co., Ltd., Shanghai, China) based on the manufacturer's instruction. The proportion (percentage) of cells within the G1, S, and G2 phase in the cell cycle of ICC cells with indicated treatment were detected by a NovoCyte2060R flow cytometer (ACEA Biosciences Inc., San Diego, CA, USA) and data were analyzed using the ACEA NovoExpress software (ACEA Biosciences Inc.).

Western blot analysis

The tissue protein was extracted using RIPA lysis buffer with protease/phosphatase inhibitor (Beyotime Biotechnology) through an electrical homogenizer KZ-II (Servicebio Technology Co., Ltd., Wuhan, China). The cell protein was extracted using RIPA lysis buffer with protease/phosphatase inhibitor (Beyotime Biotechnology). The protein concentrations were determined by the BCA protein assay (Beyotime Biotechnology). Western blot analysis were performed as previously described. Separated proteins by SDS-PAGE were transferred onto PVDF membranes (Roche, Basel, Switzerland) and incubated overnight at 4°C with the respective primary antibodies (antibody information is listed in Table S2). Then the membranes were incubated with secondary antibodies for 1 h at RT. Finally, an enhanced chemiluminescence (ECL) kit (Beyotime Biotechnology) was used to visualize the resolved proteins with a Tanon-5200 Chemiluminescent Imaging System (Tanon Science & Technology Co., Ltd., Shanghai, China).

Reverse transcription quantitative PCR assay

Total RNA was extracted using TRIzol Reagents (TransGen Biotech, Beijing, China) and was synthesized complementary DNA (cDNA) with a reverse transcriptase kit (APExBIO) following the manufacturer's instructions. Subsequently, RT-qPCR analysis was performed using SYBR Green I Master Mix kit (APExBIO). Each sample was analyzed in triplicate using a Bioer LineGene 9600 thermal cycler (Bioer Technology Co., Ltd., Hangzhou, China). The primer sequences used in this study were listed in Supporting Information Table S4.

Human ICC sample and isolation of primary ICC cells

The expression of LDLR in human ICC was analyzed using a cohort including 53 ICC patients who had undergone curative liver resection at the First Affiliated Hospital of Sun Yat-sen University and another 27 ICC specimens collected from the First Affiliated Hospital of Jinan University. The fresh ICC specimen used in PDX establishment was obtained from the First Affiliated Hospital of Jinan University and the detailed information of the patient is listed in Table S5. The use of the clinical specimens for research purposes was approved by the Jinan University Ethics Committee (ethics approval number: KY-2023-100) and IEC for Clinical Research and Animal Trials of the First Affiliated Hospital of Sun Yat-sen University (ethics approval number: 2021678) and was performed in accordance with the Declaration of Helsinki. Written informed consent was obtained from the patients. For isolation of primary ICC cells, fresh ICC tissues from ICC patients or from PDX-bearing mice were sheared into 1 mm^3 small pieces. Then the tissue fragments were further handled using a mechanical tissue homogenizer (Miltenyi, Bergisch Gladbach, Germany). After that, a single-cell suspension was obtained using a Tumor Dissociation Kit (Miltenyi) according to the manufacturer's instructions. Tumor cells were finally purified using anti-EpCAM beads (Miltenyi). Primary cells were cultured in DMEM medium supplemented with 20% FBS, 1% sodium pyruvate, 1× B27, 20 ng/mL of bFGF, 20 ng/mL of EGF, 0.5% penicillin/streptomycin, and 10 μg/mL of gentamicin at 37°C in a humidified atmosphere of 5% CO_2.

Histology, immunohistochemistry, and immunofluorescence

For histology and immunohistochemistry, formalin-fixed tissue samples of mouse or human ICC tissues were embedded in paraffin and sectioned at a thickness of 5 μm. Histology and immunohistochemistry were performed as previously described.[64] The related antibody information is listed in Table S2. Images were acquired by an Olympus BX51 Fluorescence Microscope (Tokyo, Japan). Three pathologists independently rendered the IHC scores. The staining intensity was scored as follows: 0, no staining (negative); 1, yellow (weak); 2, brownish yellow (medium); and 3, brown (strong). In the same tissue, multiple high-power fields with different staining intensities were viewed, and the percentage of cholangiocarcinoma-positive cells was calculated separately and then taken as the average. Scores for staining intensity and percentage of positive cells were then multiplied to generate the immunoreactivity score for each case. For cell immunofluorescence, cells were fixed in methanol for 15 min and blocked with 0.2% Triton X-100 in 4% BSA for 30 min at room temperature (RT), then incubated with the indicated antibodies overnight at 4°C. After that, the fluorescent secondary antibodies were added and incubated for another 1 h at RT. Nuclei were counterstained with DAPI. For

tissue immunofluorescence, tissues were embedded in OCT and cryosection of 10 μm thickness was performed in a Leica CM1860 Cryostat Microtome (Leica). All sections were socked in PBS to remove OCT, after which the slides were preincubated in 10% normal goat serum for 1 h, and then incubated with indicated primary antibodies and fluorescent secondary antibodies. Last, nuclei were counterstained with DAPI. Images were acquired with a Leica SP8 confocal microscope (Leica).

Animal studies

Five- to 7-week-old male BALB/c mice were purchased from Guangdong Medical Laboratory Animal Center (Guangzhou, China). Five- to 7-week-old male C57BL/6 mice and male BALB/c-nu mice were obtained from Ruige Biological Technology Co., Ltd (Guangzhou, China). Three- to 5-week-old male NOD-scid mice were purchased from Vital River Laboratory Animal Technology Co., Ltd (Beijing, China). All experimental animals were housed, fed, and monitored in a specific pathogen-free grade Laboratory Animal Center of Jinan University. The experimental animal protocol was reviewed and approved by the Institutional Animal Ethical Committee, Laboratory Animal Center of Jinan University, and followed by the Guide for the Care and Use of Laboratory Animals by the US National Institutes of Health. Animals were anesthetized using inhaled isoflurane gas and euthanized by CO_2 asphyxiation.

DEN-LMBDL-induced spontaneous ICC model

The construction of the DEN-LMBDL model of ICC was performed as reported.[65] To achieve tumor development in mice, we subjected 7-week-old male BALB/c mice to two separate weekly intraperitoneal injections of 100 mg/kg DEN. Then, LMBDL was performed in all experimental mice. After 2 weeks, DEN (25 mg/kg) was administered by oral gavage once a week, and the total duration of the experiment lasted 28 weeks, with ICC formation.

Akt/Yap-induced spontaneous ICC model

The genetic spontaneous ICC model based on hydrodynamic tail vein injection was performed as described previously.[41,66] Briefly, 20 μg of pT3-myr-AKT-HA plasmid, 30 μg of pT3-EF1a-YapS127A plasmid, and 4 μg of SB13 transposase-encoding plasmid were mixed in 0.9% saline solution at a final volume of 10% of the animal's body weight and injected into a C57BL/6 mouse via the tail vein within 7 s. ICC development occurred about 6 weeks later after injection.

In vivo ICC xenograft model

For subcutaneous ICC PDX, a fresh human ICC tissue was trimmed into about 20 mm^3 fragments and subcutaneously implanted in NOD-scid mice. Until tumor volume reached about 100 mm^3, xenograft-bearing mice were intratumorally injected with AAV F-A (2×10^{11} vg/mouse) once a week to induce F-A expression. After induction for 3 weeks, F-A-positive ICC PDX were aseptically excised, cut into about 20 mm^3 fragments and transferred subcutaneously into the subsequent passage mice. Once the tumor reached a mean volume of about 100 mm^3, seven mice per group were randomly allocated for indicated treatments. Tumors were measured every 4 days and tumor volume was calculated by the formula: $V = W^2 \times L/2$, where V is tumor volume, W is tumor width, and L is tumor length. For the orthotopic ICC PDX model. The subcutaneous ICC PDX tumors transfected with AAV F-A or AAV CTL as described above were sheared into 1 mm^3 small pieces. Subsequently, the small pieces were further digested into a single-cell suspension as described in "human ICC sample and isolation of primary ICC cells" section. The single-cell suspensions were then mixed 1:1 to Matrigel and then orthotopically injected into the liver subcapsular region of the middle lobe of NOD-scid mice. Randomization was conducted within 1 week after eligibility confirmation, and treatments began within 1 week thereafter. For the establishment of orthotopic CDX ICC model, BALB/c nude mice were anesthetized, and ICC cell lines were suspended in PBS with Matrigel solution (PBS: Matrigel = 1:1), then 100 μL (about 1×10^6 cells) of cell suspension were injected into the subcapsular region of the middle lobe.

RNA-seq analysis

Primary human ICC cells were extracted and transfected with lentivirus-vector or lentivirus-F-A, and then transfected with or without 200 nM of F-A Cho-HDO for 72 h. Total RNA was purified using TRIzol reagent (TransGen Biotech, Beijing, China) according to the manufacturer's instructions. RNA-seq analysis was performed by IGE Biotechnology Co., Ltd. (Guangzhou, China) using biological triplicates. StringTie and edgeR were used to assess the expression levels of all transcripts. The differentially expressed genes were selected with log2 (fold change) > 1 or log2 (fold change) <−1 and with statistical significance (p value <0.05). The GO terms (http://www.geneontology.org) of differentially expressed genes were finally annotated.

Quantification of cellular and tissue Asn level

The change in asparagine levels upon F-A Cho-HDO treatment was determined using an Asparagine Assay Kit (Abcam, Cambridge, England). Briefly, ICC cells or tissues were homogenized on ice with 100 μL of ice-cold Asparagine Assay Buffer and then centrifuged at 15,000 × *g* for 10 min at 4°C. The supernatant was transferred to a new microfuge tube and relative Asn concentrations were detected using the Asparagine Assay Kit according to the manufacturer's instructions.

ChIP-qPCR assay

Indicated ICC cells were treated with 200 nM of F-A Cho-HDO for 72 h before they were subjected to chromatin preparation for the ChIP analysis. ChIP assays were conducted using the Simple ChIP Enzymatic Chromatin IP Kit (Cell Signaling Technology, Danvers, MA, USA) according to the manufacturer's instructions. Briefly, ICC cells with indicated treatments were crosslinked with 1% formaldehyde for 20 min and terminated by addition of glycine (150 mM). Then cells were lysed, and chromatins were sonicated to an average length of 200–1,000 base pairs. One hundred microliters of chromatins were immunoprecipitated overnight at 4°C using 10 μg of anti-STAT1, non-specific anti-immunoglobulin G was served as the negative control. Then 20 μL of protein A beads was added and incubated for 2 h. After reverse cross-linking and DNA purification,

immunoprecipitated DNA was quantified by RT-qPCR. The primers used for RT-qPCR analysis of precipitated DNA are listed in Table S6.

Statistical analysis

All statistical analysis was performed using GraphPad Prism 8.0.1 (GraphPad Software, San Diego, CA). Differences between two groups were evaluated using two-tailed unpaired t test or Mann Whitney test. One-way ANOVA followed by Tukey's post hoc test was used to analyze differences among three groups or more. Overall survival analysis of mice was performed using the Kaplan-Meier method and compared using the log rank test. All data are represented as means ± SD, and a p value <0.05 was considered as statistically significant.

DATA AND CODE AVAILABILITY

The datasets used and/or analyzed during the current study are available from the corresponding author upon reasonable request.

SUPPLEMENTAL INFORMATION

Supplemental information can be found online at https://doi.org/10.1016/j.omtn.2023.102047.

ACKNOWLEDGMENTS

This work was supported by National Natural Science Foundation of China (Grant No. 82172602 to N.Y.; Grant No. 82102782 to H.Y.); Natural Science Foundation of Guangdong Province (Grant No. 2023A1515011892 to N.Y.); the Basic and Applied Basic Research Project of Guangzhou Basic Research Program (Grant No. 2023A04J1917 to J.L.); the Flagship Specialty Construction Project-General Surgery of the First Affiliated Hospital of the Jinan University (Grant No. 711003 to J.L.). The authors thank the Tin Ka Ping Medical Experimental Research Center, School of Medicine, Jinan University, for providing the facilities and assistance that supported this research.

AUTHOR CONTRIBUTIONS

N.Y., J.L., and H.Y. designed and supervised the study. Z.C., C.G., X.Z., L.L., and Y.X. performed animal experiments. Z.C. and X.Z. performed immunofluorescence and immunohistochemistry assay. Z.C. and X.Z. performed cell line studies and western blotting assay. Z.C. and B.Z. performed plasmid extraction, transfection, and RT-qPCR analysis. J.Z. provided guidance on HDO design, synthesis, and administration. J.L. and D.C. provided ICC clinical specimens and performed the analysis. N.Y., Z.C., and B.Z. analyzed the data. Z.C. and N.Y. wrote the manuscript. N.Y., J.H., H.Y., B.Z., and D.C. revised the manuscript.

DECLARATION OF INTERESTS

The authors declare no competing interests.

REFERENCES

1. Song, G., Shi, Y., Meng, L., Ma, J., Huang, S., Zhang, J., Wu, Y., Li, J., Lin, Y., Yang, S., et al. (2022). Single-cell transcriptomic analysis suggests two molecularly subtypes of intrahepatic cholangiocarcinoma. Nat. Commun. *13*, 1642.
2. Banales, J.M., Marin, J.J.G., Lamarca, A., Rodrigues, P.M., Khan, S.A., Roberts, L.R., Cardinale, V., Carpino, G., Andersen, J.B., Braconi, C., et al. (2020). Cholangiocarcinoma 2020: the next horizon in mechanisms and management. Nat. Rev. Gastroenterol. Hepatol. *17*, 557–588.
3. Reames, B.N., Bagante, F., Ejaz, A., Spolverato, G., Ruzzenente, A., Weiss, M., Alexandrescu, S., Marques, H.P., Aldrighetti, L., Maithel, S.K., et al. (2017). Impact of adjuvant chemotherapy on survival in patients with intrahepatic cholangiocarcinoma: a multi-institutional analysis. HPB (Oxford) *19*, 901–909.
4. Elvevi, A., Laffusa, A., Scaravaglio, M., Rossi, R.E., Longarini, R., Stagno, A.M., Cristoferi, L., Ciaccio, A., Cortinovis, D.L., Invernizzi, P., and Massironi, S. (2022). Clinical treatment of cholangiocarcinoma: an updated comprehensive review. Ann. Hepatol. *27*, 100737.
5. Kelley, R.K., Bridgewater, J., Gores, G.J., and Zhu, A.X. (2020). Systemic therapies for intrahepatic cholangiocarcinoma. J. Hepatol. *72*, 353–363.
6. Wang, M., Chen, Z., Guo, P., Wang, Y., and Chen, G. (2021). Therapy for advanced cholangiocarcinoma: Current knowledge and future potential. J. Cell Mol. Med. *25*, 618–628.
7. Martin-Serrano, M.A., Kepecs, B., Torres-Martin, M., Bramel, E.R., Haber, P.K., Merritt, E., Rialdi, A., Param, N.J., Maeda, M., Lindblad, K.E., et al. (2023). Novel microenvironment-based classification of intrahepatic cholangiocarcinoma with therapeutic implications. Gut *72*, 736–748.
8. Lowery, M.A., Ptashkin, R., Jordan, E., Berger, M.F., Zehir, A., Capanu, M., Kemeny, N.E., O'Reilly, E.M., El-Dika, I., Jarnagin, W.R., et al. (2018). Comprehensive Molecular Profiling of Intrahepatic and Extrahepatic Cholangiocarcinomas: Potential Targets for Intervention. Clin. Cancer Res. *24*, 4154–4161.
9. Berchuck, J.E., Facchinetti, F., DiToro, D.F., Baiev, I., Majeed, U., Reyes, S., Chen, C., Zhang, K., Sharman, R., Uson Junior, P.L.S., et al. (2022). The clinical landscape of cell-free DNA alterations in 1671 patients with advanced biliary tract cancer. Ann. Oncol. *33*, 1269–1283.
10. Ross, J.S., Wang, K., Gay, L., Al-Rohil, R., Rand, J.V., Jones, D.M., Lee, H.J., Sheehan, C.E., Otto, G.A., Palmer, G., et al. (2014). New routes to targeted therapy of intrahepatic cholangiocarcinomas revealed by next-generation sequencing. Oncol. *19*, 235–242.
11. Arai, Y., Totoki, Y., Hosoda, F., Shirota, T., Hama, N., Nakamura, H., Ojima, H., Furuta, K., Shimada, K., Okusaka, T., et al. (2014). Fibroblast growth factor receptor 2 tyrosine kinase fusions define a unique molecular subtype of cholangiocarcinoma. Hepatology *59*, 1427–1434.
12. Borad, M.J., Champion, M.D., Egan, J.B., Liang, W.S., Fonseca, R., Bryce, A.H., McCullough, A.E., Barrett, M.T., Hunt, K., Patel, M.D., et al. (2014). Integrated genomic characterization reveals novel, therapeutically relevant drug targets in FGFR and EGFR pathways in sporadic intrahepatic cholangiocarcinoma. PLoS Genet. *10*, e1004135.
13. Moeini, A., Sia, D., Bardeesy, N., Mazzaferro, V., and Llovet, J.M. (2016). Molecular Pathogenesis and Targeted Therapies for Intrahepatic Cholangiocarcinoma. Clin. Cancer Res. *22*, 291–300.
14. Chen, L., Zhang, Y., Yin, L., Cai, B., Huang, P., Li, X., and Liang, G. (2021). Fibroblast growth factor receptor fusions in cancer: opportunities and challenges. J. Exp. Clin. Cancer Res. *40*, 345.
15. Abou-Alfa, G.K., Sahai, V., Hollebecque, A., Vaccaro, G., Melisi, D., Al-Rajabi, R., Paulson, A.S., Borad, M.J., Gallinson, D., Murphy, A.G., et al. (2020). Pemigatinib for previously treated, locally advanced or metastatic cholangiocarcinoma: a multicentre, open-label, phase 2 study. Lancet Oncol. *21*, 671–684.
16. Zugman, M., Botrus, G., Pestana, R.C., and Uson Junior, P.L.S. (2022). Precision Medicine Targeting FGFR2 Genomic Alterations in Advanced Cholangiocarcinoma: Current State and Future Perspectives. Front. Oncol. *12*, 860453.
17. Silverman, I.M., Hollebecque, A., Friboulet, L., Owens, S., Newton, R.C., Zhen, H., Féliz, L., Zecchetto, C., Melisi, D., and Burn, T.C. (2021). Clinicogenomic Analysis of FGFR2-Rearranged Cholangiocarcinoma Identifies Correlates of Response and Mechanisms of Resistance to Pemigatinib. Cancer Discov. *11*, 326–339.
18. Storandt, M.H., Jin, Z., and Mahipal, A. (2022). Pemigatinib in cholangiocarcinoma with a FGFR2 rearrangement or fusion. Expert Rev. Anticancer Ther. *22*, 1265–1274.
19. Yue, S., Li, Y., Chen, X., Wang, J., Li, M., Chen, Y., and Wu, D. (2021). FGFR-TKI resistance in cancer: current status and perspectives. J. Hematol. Oncol. *14*, 23.

20. Datta, J., Damodaran, S., Parks, H., Ocrainiciuc, C., Miya, J., Yu, L., Gardner, E.P., Samorodnitsky, E., Wing, M.R., Bhatt, D., et al. (2017). Akt Activation Mediates Acquired Resistance to Fibroblast Growth Factor Receptor Inhibitor BGJ398. Mol. Cancer Therapeut. *16*, 614–624.

21. Kendre, G., Marhenke, S., Lorz, G., Becker, D., Reineke-Plaaß, T., Poth, T., Murugesan, K., Kühnel, F., Woller, N., Wirtz, R.M., et al. (2021). The Co-mutational Spectrum Determines the Therapeutic Response in Murine FGFR2 Fusion-Driven Cholangiocarcinoma. Hepatology *74*, 1357–1370.

22. Crooke, S.T., Baker, B.F., Crooke, R.M., and Liang, X.H. (2021). Antisense technology: an overview and prospectus. Nat. Rev. Drug Discov. *20*, 427–453.

23. Olie, R.A., and Zangemeister-Wittke, U. (2001). Targeting tumor cell resistance to apoptosis induction with antisense oligonucleotides: progress and therapeutic potential. Drug Resist. Updates *4*, 9–15.

24. Hu, B., Zhong, L., Weng, Y., Peng, L., Huang, Y., Zhao, Y., and Liang, X.J. (2020). Therapeutic siRNA: state of the art. Signal Transduct. Targeted Ther. *5*, 101.

25. Hara, R.I., Yoshioka, K., and Yokota, T. (2020). DNA-RNA Heteroduplex Oligonucleotide for Highly Efficient Gene Silencing. Methods Mol. Biol. *2176*, 113–119.

26. Nagata, T., Dwyer, C.A., Yoshida-Tanaka, K., Ihara, K., Ohyagi, M., Kaburagi, H., Miyata, H., Ebihara, S., Yoshioka, K., Ishii, T., et al. (2021). Cholesterol-functionalized DNA/RNA heteroduplexes cross the blood-brain barrier and knock down genes in the rodent CNS. Nat. Biotechnol. *39*, 1529–1536.

27. Tan, X., Jia, F., Wang, P., and Zhang, K. (2020). Nucleic acid-based drug delivery strategies. J. Control Release *323*, 240–252.

28. Varini, K., Lécorché, P., Sonnette, R., Gassiot, F., Broc, B., Godard, M., David, M., Faucon, A., Abouzid, K., Ferracci, G., et al. (2019). Target engagement and intracellular delivery of mono- and bivalent LDL receptor-binding peptide-cargo conjugates: Implications for the rational design of new targeted drug therapies. J. Control Release *314*, 141–161.

29. van den Boomen, D.J.H., Sienkiewicz, A., Berlin, I., Jongsma, M.L.M., van Elsland, D.M., Luzio, J.P., Neefjes, J.J.C., and Lehner, P.J. (2020). A trimeric Rab7 GEF controls NPC1-dependent lysosomal cholesterol export. Nat. Commun. *11*, 5559.

30. Osborn, M.F., and Khvorova, A. (2018). Improving siRNA Delivery In Vivo Through Lipid Conjugation. Nucleic Acid Therapeut. *28*, 128–136.

31. Miller, C.M., and Harris, E.N. (2016). Antisense Oligonucleotides: Treatment Strategies and Cellular Internalization. RNA Dis. *3*, e1393.

32. Rinaldi, C., and Wood, M.J.A. (2018). Antisense oligonucleotides: the next frontier for treatment of neurological disorders. Nat. Rev. Neurol. *14*, 9–21.

33. Xie, Y., Su, N., Yang, J., Tan, Q., Huang, S., Jin, M., Ni, Z., Zhang, B., Zhang, D., Luo, F., et al. (2020). FGF/FGFR signaling in health and disease. Signal Transduct. Targeted Ther. *5*, 181.

34. He, Y., Rodrigues, R.M., Wang, X., Seo, W., Ma, J., Hwang, S., Fu, Y., Trojnár, E., Mátyás, C., Zhao, S., et al. (2021). Neutrophil-to-hepatocyte communication via LDLR-dependent miR-223-enriched extracellular vesicle transfer ameliorates nonalcoholic steatohepatitis. J. Clin. Invest. *131*, e141513.

35. Chang, M.M., Lai, M.S., Hong, S.Y., Pan, B.S., Huang, H., Yang, S.H., Wu, C.C., Sun, H.S., Chuang, J.I., Wang, C.Y., and Huang, B.M. (2018). FGF9/FGFR2 increase cell proliferation by activating ERK1/2, Rb/E2F1, and cell cycle pathways in mouse Leydig tumor cells. Cancer Sci. *109*, 3503–3518.

36. Dong, L., Lu, D., Chen, R., Lin, Y., Zhu, H., Zhang, Z., Cai, S., Cui, P., Song, G., Rao, D., et al. (2022). Proteogenomic characterization identifies clinically relevant subgroups of intrahepatic cholangiocarcinoma. Cancer Cell *40*, 70–87.e15.

37. Lovitt, C.J., Shelper, T.B., and Avery, V.M. (2014). Advanced cell culture techniques for cancer drug discovery. Biology *3*, 345–367.

38. Zhang, H.E., Henderson, J.M., and Gorrell, M.D. (2019). Animal models for hepatocellular carcinoma. Biochim. Biophys. Acta, Mol. Basis Dis. *1865*, 993–1002.

39. Sato, K., Marzioni, M., Meng, F., Francis, H., Glaser, S., and Alpini, G. (2019). Ductular Reaction in Liver Diseases: Pathological Mechanisms and Translational Significances. Hepatology *69*, 420–430.

40. Wang, J., Dong, M., Xu, Z., Song, X., Zhang, S., Qiao, Y., Che, L., Gordan, J., Hu, K., Liu, Y., et al. (2018). Notch2 controls hepatocyte-derived cholangiocarcinoma formation in mice. Oncogene *37*, 3229–3242.

41. Song, X., Xu, H., Wang, P., Wang, J., Affo, S., Wang, H., Xu, M., Liang, B., Che, L., Qiu, W., et al. (2021). Focal adhesion kinase (FAK) promotes cholangiocarcinoma development and progression via YAP activation. J. Hepatol. *75*, 888–899.

42. Gao, Y., Wang, P.X., Cheng, J.W., Sun, Y.F., Hu, B., Guo, W., Zhou, K.Q., Yin, Y., Li, Y.C., Wang, J., et al. (2019). Chemotherapeutic perfusion of portal vein after tumor thrombectomy and hepatectomy benefits patients with advanced hepatocellular carcinoma: A propensity score-matched survival analysis. Cancer Med. *8*, 6933–6944.

43. Kulkarni, J.A., Witzigmann, D., Thomson, S.B., Chen, S., Leavitt, B.R., Cullis, P.R., and van der Meel, R. (2021). The current landscape of nucleic acid therapeutics. Nat. Nanotechnol. *16*, 630–643.

44. Bishani, A., and Chernolovskaya, E.L. (2021). Activation of Innate Immunity by Therapeutic Nucleic Acids. Int. J. Mol. Sci. *22*, 13360.

45. Shukla, S., Chen, Z.S., and Ambudkar, S.V. (2012). Tyrosine kinase inhibitors as modulators of ABC transporter-mediated drug resistance. Drug Resist. Updates *15*, 70–80.

46. Wang, X., Jiang, W., Du, Y., Zhu, D., Zhang, J., Fang, C., Yan, F., and Chen, Z.S. (2022). Targeting feedback activation of signaling transduction pathways to overcome drug resistance in cancer. Drug Resist. Updates *65*, 100884.

47. Greco, A., Gong, S.S., Ittmann, M., and Basilico, C. (1989). Organization and expression of the cell cycle gene, ts11, that encodes asparagine synthetase. Mol. Cell Biol. *9*, 2350–2359.

48. Deng, L., Yao, P., Li, L., Ji, F., Zhao, S., Xu, C., Lan, X., and Jiang, P. (2020). p53-mediated control of aspartate-asparagine homeostasis dictates LKB1 activity and modulates cell survival. Nat. Commun. *11*, 1755.

49. Silverman, L.B., Supko, J.G., Stevenson, K.E., Woodward, C., Vrooman, L.M., Neuberg, D.S., Asselin, B.L., Athale, U.H., Clavell, L., Cole, P.D., et al. (2010). Intravenous PEG-asparaginase during remission induction in children and adolescents with newly diagnosed acute lymphoblastic leukemia. Blood *115*, 1351–1353.

50. Covini, D., Tardito, S., Bussolati, O., Chiarelli, L.R., Pasquetto, M.V., Digilio, R., Valentini, G., and Scotti, C. (2012). Expanding targets for a metabolic therapy of cancer: L-asparaginase. Recent Pat. Anti-Cancer Drug Discov. *7*, 4–13.

51. Wu, Q., Zhen, Y., Shi, L., Vu, P., Greninger, P., Adil, R., Merritt, J., Egan, R., Wu, M.J., Yin, X., et al. (2022). EGFR Inhibition Potentiates FGFR Inhibitor Therapy and Overcomes Resistance in FGFR2 Fusion-Positive Cholangiocarcinoma. Cancer. Discov. *12*, 1378–1395.

52. Pu, X., Ye, Q., Cai, J., Yang, X., Fu, Y., Fan, X., Wu, H., Chen, J., Qiu, Y., and Yue, S. (2021). Typing FGFR2 translocation determines the response to targeted therapy of intrahepatic cholangiocarcinomas. Cell Death Dis. *12*, 256.

53. Borad, M.J., Gores, G.J., and Roberts, L.R. (2015). Fibroblast growth factor receptor 2 fusions as a target for treating cholangiocarcinoma. Curr. Opin. Gastroenterol. *31*, 264–268.

54. Sun, Y., Lau, S.Y., Lim, Z.W., Chang, S.C., Ghadessy, F., Partridge, A., and Miserez, A. (2022). Phase-separating peptides for direct cytosolic delivery and redox-activated release of macromolecular therapeutics. Nat. Chem. *14*, 274–283.

55. Quemener, A.M., Bachelot, L., Forestier, A., Donnou-Fournet, E., Gilot, D., and Galibert, M.D. (2020). The powerful world of antisense oligonucleotides: From bench to bedside. Wiley. Interdiscip. Rev. RNA. *11*, e1594.

56. Ono, D., Asada, K., Yui, D., Sakaue, F., Yoshioka, K., Nagata, T., and Yokota, T. (2021). Separation-related rapid nuclear transport of DNA/RNA heteroduplex oligonucleotide: unveiling distinctive intracellular trafficking. Mol. Ther. Nucleic Acids *23*, 1360–1370.

57. Asami, Y., Nagata, T., Yoshioka, K., Kunieda, T., Yoshida-Tanaka, K., Bennett, C.F., Seth, P.P., and Yokota, T. (2021). Efficient Gene Suppression by DNA/DNA Double-Stranded Oligonucleotide In Vivo. Mol. Ther. *29*, 838–847.

58. Cools, J., Maertens, C., and Marynen, P. (2005). Resistance to tyrosine kinase inhibitors: calling on extra forces. Drug Resist. Updates *8*, 119–129.

59. Chiu, M., Taurino, G., Bianchi, M.G., Kilberg, M.S., and Bussolati, O. (2019). Asparagine Synthetase in Cancer: Beyond Acute Lymphoblastic Leukemia. Front. Oncol. *9*, 1480.

60. Noree, C., Monfort, E., and Shotelersuk, V. (2018). Human asparagine synthetase associates with the mitotic spindle. Biol. Open *7*, bio038307.

61. Li, Z., Cheng, D., Mon, H., Zhu, L., Xu, J., Tatsuke, T., Lee, J.M., Xia, Q., and Kusakabe, T. (2013). Cell cycle-dependent recruitment of polycomb proteins to the ASNS promoter counteracts C/ebp-mediated transcriptional activation in Bombyx mori. PLoS One *8*, e52320.

62. Martins Cavaco, A.C., Dâmaso, S., Casimiro, S., and Costa, L. (2020). Collagen biology making inroads into prognosis and treatment of cancer progression and metastasis. Cancer Metastasis Rev. *39*, 603–623.

63. Chou, T.C. (2010). Drug combination studies and their synergy quantification using the Chou-Talalay method. Cancer Res. *70*, 440–446.

64. Gao, C.Q., Chu, Z.Z., Zhang, D., Xiao, Y., Zhou, X.Y., Wu, J.R., Yuan, H., Jiang, Y.C., Chen, D., Zhang, J.C., et al. (2023). Serine/threonine kinase TBK1 promotes cholangiocarcinoma progression via direct regulation of β-catenin. Oncogene *42*, 1492–1507.

65. Yang, H., Li, T.W.H., Peng, J., Tang, X., Ko, K.S., Xia, M., and Aller, M.A. (2011). A mouse model of cholestasis-associated cholangiocarcinoma and transcription factors involved in progression. Gastroenterology *141*, 378–388.e1-4.

66. Chen, X., and Calvisi, D.F. (2014). Hydrodynamic transfection for generation of novel mouse models for liver cancer research. Am. J. Pathol. *184*, 912–923.